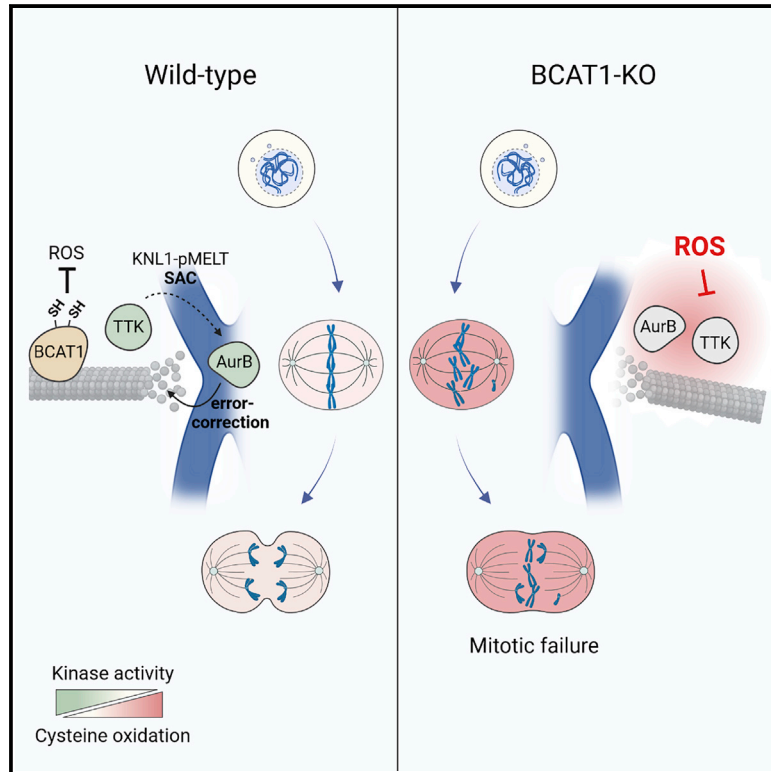


# BCAT1 redox function maintains mitotic fidelity

## Graphical abstract



## Authors

Liliana Francois, Pavle Boskovic, Julian Knerr, ..., Robert Grosse, Peter Lichter, Bernhard Radlwimmer

## Correspondence

b.radlwimmer@dkfz.de

## In brief

Francois et al. show that the metabolic enzyme BCAT1 has a moonlighting function in mitosis that requires its redox-active CXXC motif. BCAT1 interacts with components of the spindle and kinetochore, prevents cysteine oxidation, and modulates the activity of mitotic kinases to sustain mitotic fidelity.

## Highlights

- BCAT1 interacts with mitotic spindle and kinetochore proteins
- BCAT1 CXXC redox motif is essential for controlling protein oxidation in mitosis
- BCAT1 sustains mitotic kinase activity
- BCAT1 CXXC motif maintains AURKB centromere localization and mitotic fidelity



## Article

# BCAT1 redox function maintains mitotic fidelity

Liliana Francois,<sup>1,6</sup> Pavle Boskovic,<sup>1,5,6</sup> Julian Knerr,<sup>2</sup> Wei He,<sup>3</sup> Gianluca Sigismondo,<sup>4</sup> Carsten Schwan,<sup>2</sup> Tushar H. More,<sup>3</sup> Magdalena Schlotter,<sup>1</sup> Jeroen Krijgsvelde,<sup>4</sup> Karsten Hiller,<sup>3</sup> Robert Grosse,<sup>2</sup> Peter Lichter,<sup>1</sup> and Bernhard Radlwimmer<sup>1,7,\*</sup>

<sup>1</sup>Division of Molecular Genetics, German Cancer Research Center (DKFZ), 69120 Heidelberg, Germany

<sup>2</sup>Institute of Pharmacology, University of Freiburg, 79102 Freiburg, Germany

<sup>3</sup>Integrated Center of Systems Biology (BRICS), Technische Universität Braunschweig, and Computational Biology of Infection Research, Helmholtz Centre for Infection Research, Braunschweig, 38092 Braunschweig, Germany

<sup>4</sup>Division of Proteomics of Stem Cells and Cancer, German Cancer Research Center (DKFZ), 69120 Heidelberg, Germany

<sup>5</sup>Faculty of Biosciences, Heidelberg University, 69120 Heidelberg, Germany

<sup>6</sup>These authors contributed equally

<sup>7</sup>Lead contact

\*Correspondence: [b.radlwimmer@dkfz.de](mailto:b.radlwimmer@dkfz.de)

<https://doi.org/10.1016/j.celrep.2022.111524>

## SUMMARY

The metabolic enzyme branched-chain amino acid transaminase 1 (BCAT1) drives cell proliferation in aggressive cancers such as glioblastoma. Here, we show that BCAT1 localizes to mitotic structures and has a non-metabolic function as a mitotic regulator. Furthermore, BCAT1 is required for chromosome segregation in cancer and induced pluripotent stem cells and tumor growth in human cerebral organoid and mouse syngraft models. Applying gene knockout and rescue strategies, we show that the BCAT1 CXXC redox motif is crucial for controlling cysteine sulfenylation specifically in mitotic cells, promoting Aurora kinase B localization to centromeres, and securing accurate chromosome segregation. These findings offer an explanation for the well-established role of BCAT1 in promoting cancer cell proliferation. In summary, our data establish BCAT1 as a component of the mitotic apparatus that safeguards mitotic fidelity through a moonlighting redox functionality.

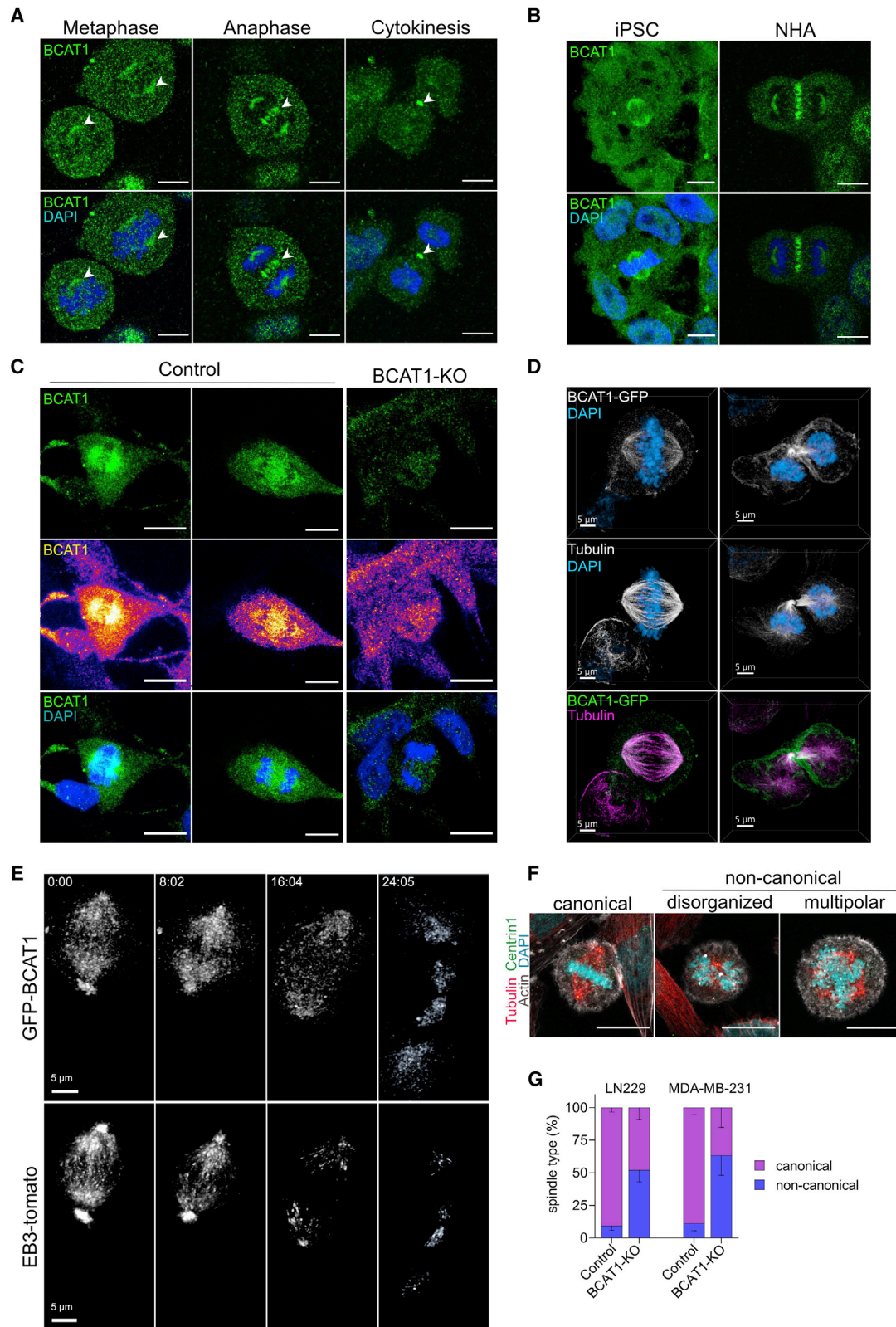
## INTRODUCTION

The cytosolic metabolic enzyme branched-chain amino acid transaminase 1 (BCAT1) catalyzes the transfer of the  $\alpha$ -amino group of the branched-chain amino acids (BCAAs) valine, leucine, and isoleucine to  $\alpha$ -ketoglutarate ( $\alpha$ -KG), generating glutamate and the respective branched-chain  $\alpha$ -ketoacids (Ichi-hara and Koyama, 1966; Taylor and Jenkins, 1966). This constitutes the first step of BCAA catabolism. BCAT1 expression is limited to embryonic and a small number of differentiated tissues, including the brain (Garcia-Espinosa et al., 2007; Sweatt et al., 2004), where BCAAs serve as a major source of nitrogen for neurotransmitter glutamate synthesis (Hutson et al., 2005). We previously showed that BCAT1 is required to sustain cell proliferation in glioblastoma, the most common and deadly malignant brain tumor in adults (Tönjes et al., 2013). Subsequent studies showed that BCAT1 supports tumor cell proliferation and invasiveness in other aggressive cancers, including leukemia, breast, and lung cancer (Hattori et al., 2017; Mayers et al., 2016; McBrayer et al., 2018; Raffel et al., 2017; Silva et al., 2017; Thewes et al., 2017; Wang et al., 2019; Zhou et al., 2013). Furthermore, BCAT1 was identified as a marker of adverse prognosis and metastatic potential in additional malignancies (de Bont et al., 2008; Yoshikawa et al., 2006; also see reviews, Ananieva and Wilkinson, 2018; Sivanand and Vander Heiden, 2020).

Despite the considerable body of work supporting the importance of BCAT1 in cancer, its mode of action has not been conclusively defined. Several mechanisms have been proposed, which assign distinct roles to each of the BCAT1 metabolites in either tumor or stroma cells. Glutamate has been reported to support tumor growth by contributing to nucleotide synthesis and glutathione production (Mayers et al., 2016; McBrayer et al., 2018; Wang et al., 2019). Branched-chain ketoacids were implicated in immune suppression (Silva et al., 2017) and support tumor cell anabolism (Zhu et al., 2020). BCAT1-generated leucine was proposed to increase cell proliferation through activation of mTOR pathway (Gu et al., 2019; Hattori et al., 2017) and depletion of  $\alpha$ -ketoglutarate to induce oncogenic chromatin modifications and hypoxic signaling (Raffel et al., 2017).

Biochemical characterization of BCAT1 identified a redox-active CXXC amino acid motif at positions C335 to C338, whose oxidation resulted in a loss of up to 50% of transaminase activity (Conway et al., 2008). The catalytic activity can be regenerated by glutaredoxin, which, together with glutathione and glutathione reductase, forms one of the major systems for cellular redox regulation (Lillig et al., 2008), suggesting that the CXXC motif acts as a redox switch (Conway et al., 2008). Consistent with this hypothesis, BCAT1 redox potential was estimated to be within the range typical for proliferating cells (Coles et al., 2012), and a subsequent study provided direct evidence that BCAT1 has thiol-disulfide oxidoreductase activity (El Hindy





(legend on next page)

et al., 2014). However, the biological relevance of this activity has not yet been evaluated in a physiologic, cellular context (Conway, 2020).

Cancers extensively reprogram mechanisms of cell cycle control, cellular metabolism, and antioxidant defense to sustain biosynthesis and cell proliferation while maintaining redox homeostasis (Zhu and Thompson, 2019). To cope with increased oxidative stress caused by rapid growth, cancer cells commonly upregulate the antioxidant enzymes thioredoxin, glutaredoxin, and peroxiredoxin, which scavenge reactive oxygen species (ROS) and facilitate redox signaling, frequently mediated by di-thiol CXXC amino acid motifs (Hanschmann et al., 2013; Hayes et al., 2020; Sies and Jones, 2020).

Thiol-based redox signaling modulates the activity of kinases and phosphatases, effectively connecting ROS with the regulation of physiological processes by phospho-signaling (Karisch et al., 2011; Leslie et al., 2003; Shao et al., 2014). Mitosis is central to malignant growth and is tightly controlled by a well-characterized phospho-signaling cascade, starting with active cyclin-dependent kinase 1 (CDK1) triggering the assembly of the spindle and proper kinetochore-spindle attachment (Heim et al., 2017). Recent studies have demonstrated the importance of redox signaling for cell division. Elevation of cellular ROS was shown to promote S-phase entry and mitotic progression (Havens et al., 2006) by targeting thiols of phosphatases and kinases (Kirova et al., 2022; Byrne et al., 2020; Lim et al., 2015, 2020). Conversely, metaphase-to-anaphase transition and successful chromosome segregation require the dephosphorylation of several mitotic targets (Hafner et al., 2014; Su et al., 2016; Wu et al., 2009).

Here, we provide evidence for a function of BCAT1 as a mitotic regulator in cancer and pluripotent stem cells, controlling cysteine oxidation and mitotic fidelity through a CXXC motif-dependent mechanism.

## RESULTS

### BCAT1 localizes to mitotic structures

To learn more about BCAT1 oncogenic function, we analyzed its subcellular localization in tumor cells by immunofluorescence and confocal imaging using three different antibodies. In dividing cells, BCAT1 unexpectedly localized to mitotic structures, including the spindle, the midzone, and the midbody in glioblas-

toma (U251, U87, and LN229), mammary carcinoma (MDA-MB-231), and osteosarcoma (U2OS) cell lines (Figures 1A and S1A). We extended these observations to non-cancer cells, including human induced pluripotent stem cells (iPSCs) and immortalized human astrocytes (Figure 1B), and we controlled for nonspecific antibody binding using BCAT1 knockout (BCAT1-KO) cells (Figure 1C). Furthermore, we ectopically expressed GFP-tagged BCAT1 (GFP-BCAT1) in LN229 cells to confirm signal specificity. Consistent with immunofluorescence, GFP-BCAT1 located to mitotic structures and redistributed from the spindle to the midbody during cell division (Figure 1D), mimicking the distribution of the tubulin-binding protein EB3 (Figure 1E and Video S1). These data suggest a function of BCAT1 in mitosis. Additional analysis of BCAT1 distribution in interphase of cancer cells *in vitro* and in xenograft tumors revealed cytoplasmic and nuclear localization (Figures S1B–S1D).

To investigate the role of BCAT1 at the mitotic spindle, we generated BCAT1-KO glioblastoma (U251 and LN229) and breast cancer (MDA-MB-231) cell lines using CRISPR-Cas9 technology. The BCAT1-KO tumor cell lines showed altered cell morphology, impaired cell migration and invasion, and reduced cell proliferation (Figures S2A–S2H), consistent with previous reports (Thewes et al., 2017; Tönjes et al., 2013; Zhou et al., 2013). Spindle morphology analysis revealed abnormal spindles with multiple or poorly defined poles with disorganized microtubules in 65% of LN229 BCAT1-KO and 75% of MDA-MB-231 BCAT1-KO cells (Figures 1F and 1G). In addition, we analyzed spindle position symmetry, which is essential for chromosome segregation (Lancaster and Baum, 2014). Recording the hemispheric tubulin fluorescence and DAPI signals, we found significant ( $p < 0.05$ ; two-sided t test) spindle and DNA-distribution asymmetries in BCAT1-KO cells (Figures S2I and S2J and Video S2).

### BCAT1 maintains mitotic fidelity in cancer and stem cells *in vitro*

Aiming to detect whether BCAT1 played a role in mitosis progression, we performed time-lapse imaging of LN229 control and BCAT1-KO cells and measured the time from the breakdown of the nuclear envelope to the onset of anaphase. We found that the majority (>60%) of LN229 control cells completed mitosis within 1 h, while BCAT1-KO required three times longer (Figures 2A and 2B). Furthermore, we observed that BCAT1-KO cells experienced a significantly ( $p = 0.034$ ; two-sided

#### Figure 1. BCAT1 localizes to mitotic structures

(A) BCAT1 is observed at the spindle (metaphase), cleavage furrow (anaphase), and midbody (cytokinesis) in glioblastoma U251 cells. Scale bar represents 10  $\mu$ m. Cells were stained against BCAT1 with a mouse monoclonal antibody (BD Biosciences).

(B) Immunofluorescence of BCAT1 in human induced pluripotent stem cells (iPSC) and a human astrocyte cell line (NHA). Scale bar represents 10  $\mu$ m. NHA were stained against BCAT1 using monoclonal mouse antibody (BD Biosciences). iPSCs were stained against BCAT1 with a rabbit polyclonal antibody provided by Myra Conway.

(C) Immunofluorescence against BCAT1 confirmed efficient knockdown and specificity of the staining (only a faint background signal is detected). Image with false colors was generated in Fiji using the “Fire” LUTs and is used to highlight the strong enrichment of BCAT1 at the spindle of control cells. Scale bar represents 10  $\mu$ m.

(D) LN229 cells transfected with GFP-BCAT1 were fixed and stained against tubulin. Representative images show co-localization of GFP-BCAT1 with tubulin at the spindle and midbody.

(E) Representative time-lapse images of LN229 cells expressing GFP-BCAT1 and the tubulin-binding protein EB3-tomato.

(F and G) Morphological features of mitotic spindles in LN229 control or BCAT1-KO cells. (F) Representative images of the different types of spindles observed and (G) frequency of occurrence in LN229 (control,  $n = 62$ ; BCAT1-KO,  $n = 69$ ) and MDA-MB-231 (control,  $n = 23$ ; BCAT1-KO,  $n = 33$ ) cells. Fixed samples were imaged with Leica SP8 confocal microscope (A–C) or Zeiss LSM800 equipped with Airyscan (D and F). Live-cell imaging of GFP-BCAT1 (E) was performed in a Zeiss LSM800 equipped with Airyscan. Image processing was done with Fiji, and videos were generated with Imaris. See also Figure S1 and Videos S1 and S2.



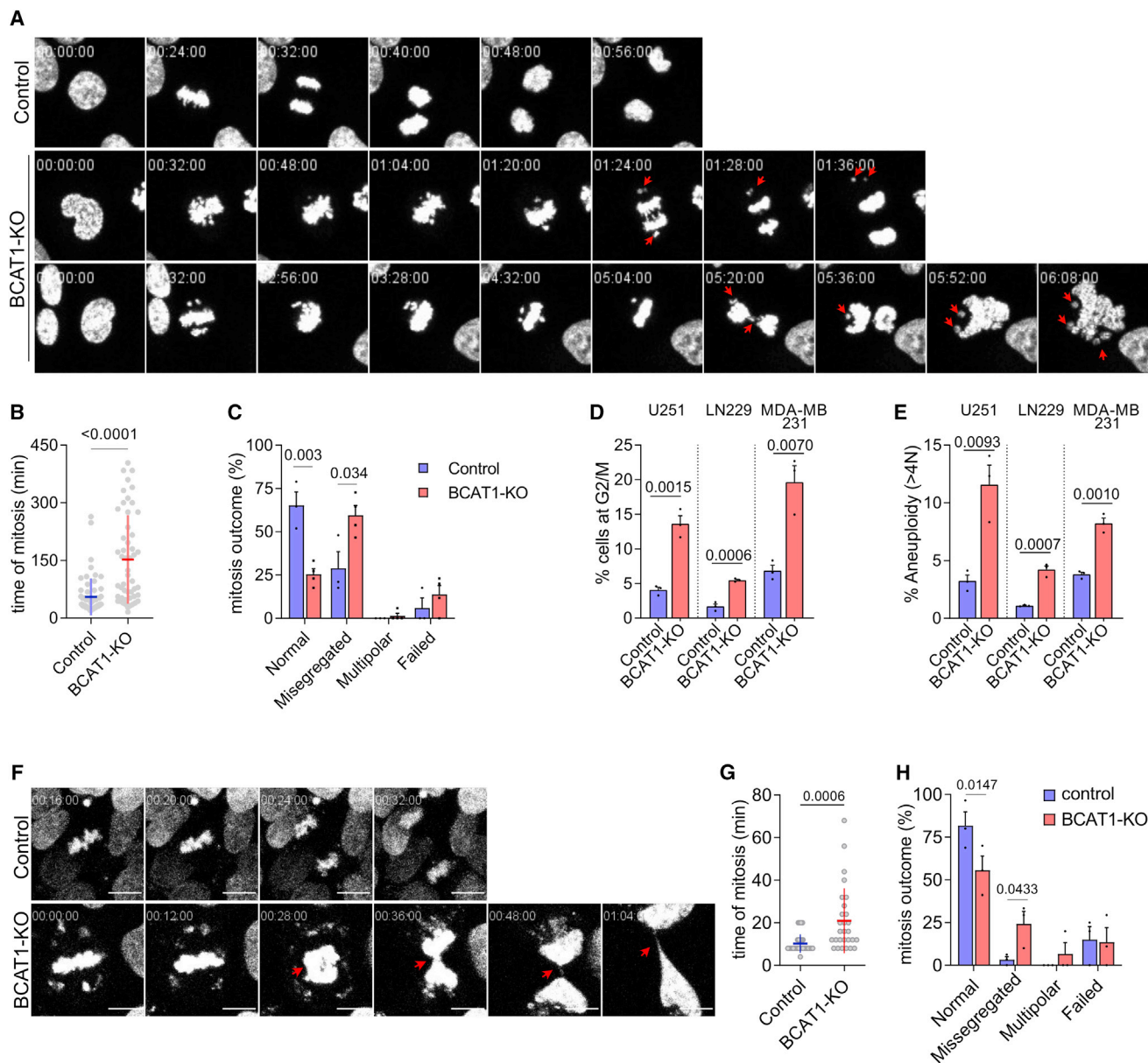


**Figure 2. BCAT1 maintains mitotic fidelity in cancer and stem cells**

(A) Representative time-lapse images showing LN229 control cells undergoing complete mitosis in  $\sim 1$  h, and two examples of LN229 BCAT1-KO cells presenting lagging chromosomes (red arrows) and leading to micronuclei and multinucleated cells.

(B) Time measured from nuclear envelop breakdown to anaphase. LN229 control,  $n = 61$  cells, average speed =  $55.2 \pm 6.1$  min; LN229 BCAT1-KO,  $n = 51$ , average speed =  $152.5 \pm 16.12$  min.

(C) Mitosis outcomes observed in LN229 control and LN229 BCAT1-KO cells. Normal: chromosomes are efficiently segregated with no observable lagging or chromosomal bridge. Missegreated: either lagging chromosomes or chromosomal bridges were observed often leading to micronuclei and/or multi-nuclei. Multipolar: chromosomes were segregated into three or more directions. Failed: no observable segregation, causing either multinucleated cells or death. Control,  $n = 61$ ; BCAT1-KO,  $n = 56$ .

(D) Percentage of cells at G2/M in three tumor cell lines (U251, LN229 = glioblastoma, MDA-MB-231 = breast carcinoma) analyzed by flow cytometry using EdU incorporation and DNA staining.

(E) Quantification of aneuploidy in the different tumor cell lines. Aneuploidy was determined by flow cytometry using propidium iodide staining.

(F) Representative time-lapse images showing an iPSC control cell undergoing normal mitosis, and an iPSC BCAT1-KO cell presenting non-segregated chromosomes (red arrows) leading to anaphase bridges. Scale bar represents 10  $\mu$ m.

(G) Time measured from onset of metaphase until anaphase in iPSCs. Control,  $n = 29$  cells, average speed =  $10 \pm 0.8$  min; BCAT1-KO,  $n = 28$  cells, average speed =  $21 \pm 2.8$  min.

(legend continued on next page)

t test) higher frequency of missegregated chromosomes, namely lagging chromosomes and chromosomes bridges that often led to the formation of micronuclei and/or multinucleated cells (Figure 2C and Video S3). Consistent with these observations, using cell cycle analysis, we detected a significant ( $p \leq 0.01$ ; two-sided t test) accumulation of cells at G2/M phase and a significant ( $p \leq 0.01$ ; two-sided t test) increase in aneuploidy of BCAT1-KO cells compared with controls. These effects were apparent in U251, LN229, and MDA-MB-231 cells (Figures 2D, 2E, and S3A–S3D), indicating that BCAT1 plays a role during mitosis in different cancer cells.

We then wondered whether BCAT1 could be also important for fast proliferating non-tumor cells, such as iPSCs, in which we also observed strong BCAT1 localization at the spindle. A significant ( $p = 0.0383$ , two-sided t test) impact in proliferation and G2/M arrest (Figures S3E–S3H) was readily detected upon BCAT1 depletion. Also consistent with our findings in cancer cells, knockout of BCAT1 in iPSCs significantly ( $p = 0.0006$ ; two-sided t test) prolonged mitotic progression (Figures 2F and 2G). Moreover, in contrast to control iPSCs, which accomplish mitosis with high fidelity (>80% completed mitosis), BCAT1-KO iPSCs experienced a significant ( $p = 0.0433$ ; two-sided t test) increase in chromosomal missegregations (Figures 2F–2H and Video S4).

These results suggest that BCAT1 contributes to mitotic fidelity in fast-dividing cells, such as cancer cells and iPSCs.

### BCAT1 is essential for tumor cell division *in situ* and *in vivo*

We next analyzed mitotic tumor cells growing in glioma cerebral organoids (GLICO), as a model of patient tumors (Linkous et al., 2019). Compared with fixed material from tumor-transplantation animal models, the GLICO model offers the advantage that the spatiotemporal dynamics of spindle structures in mitotic cells can be directly observed by live-cell imaging.

Mature (DIV > 25) cerebral organoids were generated from iPSCs, and their organization was confirmed by the expression and spatial organization of typical markers such as NES, TUBB3, and SOX2, as well as the presence of a dividing Ki67-positive population of cells in subventricular-like zones (Figures 3A and S4). Then, we co-cultured the organoids with GFP-expressing LN229 control or BCAT1-KO cells that were previously maintained in stem cell enrichment spheroid culture. Within 10 to 14 days, LN229 control cells invaded a large portion of the organoids, whereas BCAT1-KO cells grew in nodules predominantly on the surface (Figure S4). To monitor spindle morphology and chromosome segregation in individual tumor cells, we performed live-cell confocal imaging of GLICOs stained with low concentrations of SiR-tubulin and SPY55-DNA (Figure 3B). In agreement with our observations *in vitro*, the majority (>80%) of BCAT1-KO tumor cells failed to assemble canonical spindles (Figure S4D) and experienced a significant ( $p = 0.0393$ , two-sided t test) increase of missegregated chromosomes during mitosis (Figures 3C and 3D and Video S5).

Together, these data indicate that BCAT1 plays a role during mitosis relevant for 2D and 3D human cell cultures.

To confirm BCAT1's physiological relevance *in vivo*, we utilized a stem cell-derived syngeneic glioblastoma mouse model that faithfully recapitulates properties of human glioblastomas, including invasive behavior, necrosis, and formation of the microvasculature (Costa et al., 2021). Control and Bcat1-KO mGB2 mouse glioblastoma cells expressing GFP and Luciferase were injected orthotopically into BL6 mice, and tumor growth was followed by bioluminescence imaging. In the control group, seven of eight animals developed large tumors and had to be sacrificed within 50–60 days. In contrast, tumor growth was apparent in only one of eight animals injected with Bcat1-KO mGB2 cells; furthermore, this tumor developed slowly and remained asymptomatic until the experiment was concluded more than 100 days post-injection. This pronounced Bcat1-dependent tumor growth difference was associated with a highly significant ( $p = 0.0004$ ; log rank test) survival advantage of mice transplanted with Bcat1-KO tumor cells (Figures 3E–3G).

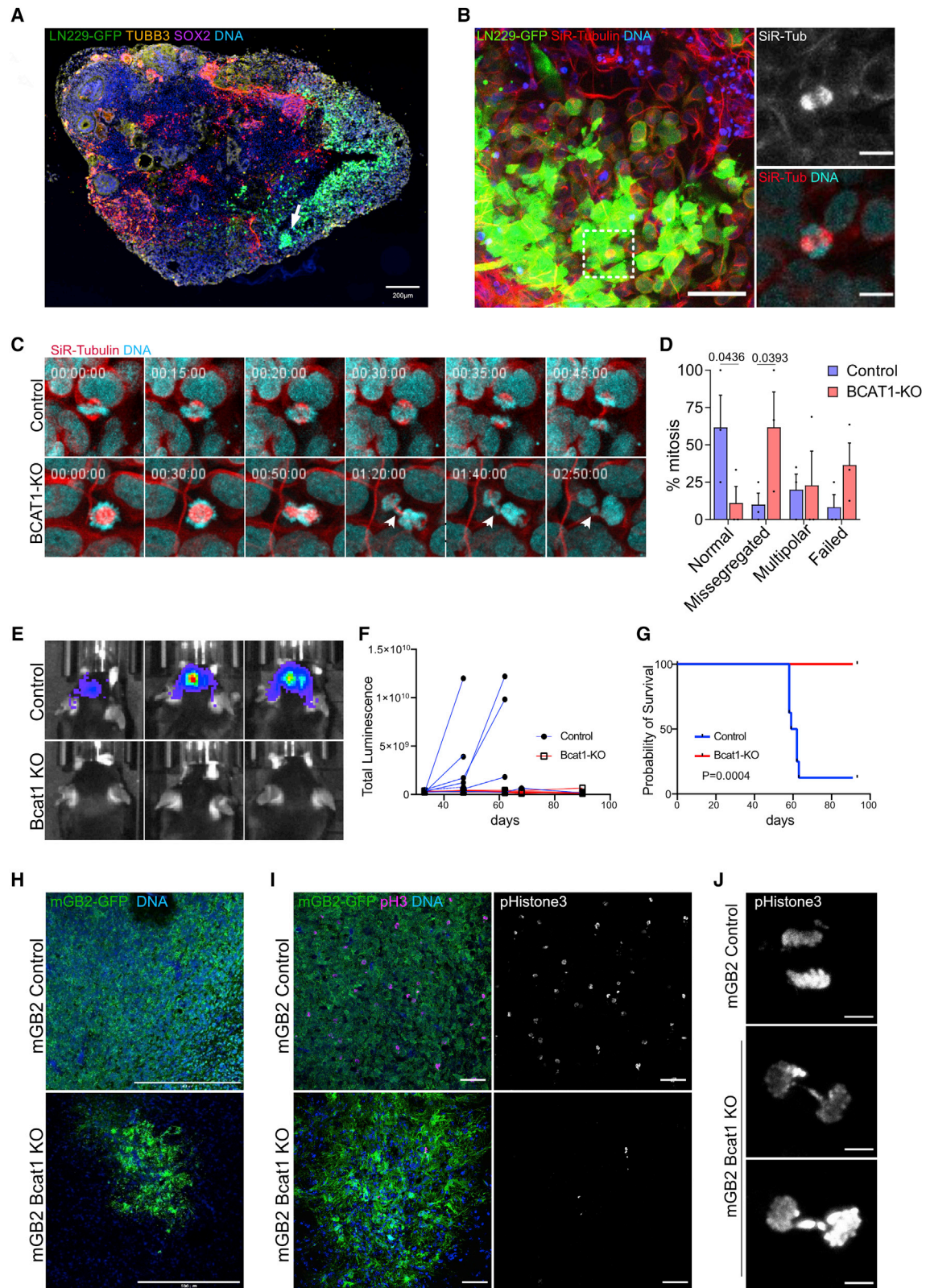
To confirm the tumor cell engraftment in the mice transplanted with Bcat1-KO tumor cells, we prepared 15- $\mu$ m sections of the entire brains of three mice. Although bioluminescence imaging had not detected tumors, we detected small GFP-positive regions in each animal by fluorescence microscopy (Figure 3H). This finding suggests that Bcat1-KO tumor cells retained the ability to engraft but failed to develop into tumors in an *in vivo* setting. To investigate whether this could be due to deficient cell division, we stained histological sections for the mitotic marker phospho-S10 in histone H3 (pH3) and anti-GFP for tumor cell identification. Control mGB2 tumors exhibited a high density of pH3-positive cells, while only a few pH3-positive cells were observed within the small populations of Bcat1-KO cells (Figure 3I). Due to the low number of mitotic Bcat1-KO cells, we could not perform a quantitative analysis of mitotic defects in Bcat1-KO cells *in vivo*. However, mGB2 control cells appeared to undergo normal mitosis, whereas Bcat1-KO mGB2 cells showed lagging chromosomes or anaphase bridges, indicating mitotic defects (Figure 3J).

### BCAT1 associates and modulates SAC-regulatory components

The analyses presented in Figures 1, 2, and 3 indicate that BCAT1 localizes to mitotic structures and has an essential function in cancer and normal cell mitosis. However, the mechanism through which it affects mitotic fidelity remains unclear.

To identify possible direct interactions of BCAT1 with mitotic regulators, we performed HA-tag immunoprecipitation and mass spectrometry (IP-MS) analysis of mitotic U251 cells stably expressing HA-BCAT1. Pre-ranked GSEA analysis of bound vs. input fractions revealed strong enrichment of proteins associated with the G2-to-M checkpoint ( $NES = 2.28$ ,  $p < 0.01$ ) and the mitotic spindle ( $NES = 1.97$ ,  $p < 0.01$ ) (Figure 4A). Furthermore, we mapped HA-BCAT1-bound (red) and unbound (blue) proteins identified in the immunoprecipitation and input samples

(H) Frequency of normal mitosis or types of mitotic abnormalities observed in control and BCAT1-KO iPSCs. Control,  $n = 49$  cells; BCAT1-KO,  $n = 37$  cells. In (B) and (G), dots represent individual cells imaged over at least three biological replicates. Bars in (C), (D), (E), and (F) are mean values  $\pm$  SEM of at least three biological replicates.  $p$  values were calculated using an unpaired, two-sided Student's t test. See also Figure S3 and Videos S3 and S4.



(legend on next page)



onto a network plot of proteins involved in mitotic spindle assembly and kinetochore function, showing that the majority interact with BCAT1 (Figure 4B). In addition, we independently validated the interactions of BCAT1 with the BUB1 mitotic checkpoint serine/threonine kinase B (BUB1B, also known as BubR1), the protein phosphatase 1 (PP1), and the spindle protein tubulin by co-immunoprecipitation (Co-IP) and western blot analysis (Figure 4C). These data indicate that BCAT1 directly interacts with structural and regulatory mitotic proteins, characterizing it as a mitotic spindle and kinetochore component.

Mitosis is regulated by complex signaling cascades involving the timely and spatially coordinated phosphorylation and dephosphorylation of mitotic regulators (Heim et al., 2017). By IP-MS analysis, we had identified multiple mitotic kinases and phosphatases, suggesting their activity might be affected by BCAT1 binding. To address this question, we performed phosphoproteomic analysis of control and BCAT1-KO mitotic LN229 and U251 cells. After confirming mitotic-cell enrichment (Figures S5A and S5B) and quantifying phospho-sites, we applied phospho-site-specific signature analysis based on the post-translational modification signature database PTMSigDB (Krug et al., 2019). Single-sample GSEA analysis identified significant depletion of the TTK (or MPS1), PLK1, and AURKB phospho-site signatures in mitotic LN229 BCAT1-KO relative to control cells (Figures 4D and S5C). These kinases are central for assuring mitotic fidelity through the spindle assembly checkpoint (SAC) and the error correction of microtubule-kinetochore attachments (Pachis and Kops, 2018; van der Waal et al., 2012). Additional kinase substrate-level analysis using the RoKAI R package (Yilmaz et al., 2021) confirmed the relative downregulation of SAC kinases in BCAT1-KO cells (Figure 4E). Analogous analysis of U251 cell line phospho-site data supported this conclusion (Figure S5D). To independently validate our phosphoproteomics data, we analyzed the extent of MELT repeat phosphorylation in KNL1 (KNL1-pMELT), an important target of TTK. KNL1-pMELT generates docking sites for the recruitment of BUB1, BUB3, and BUB1B, and it is essential for activation of the SAC and error correction mechanisms (Manic et al., 2017; Vleugel et al., 2015; Zhang et al., 2014). Immunofluorescence using a specific KNL1-pMELT (T943/1155) antibody

showed significant ( $p < 0.0001$ , two-sided  $t$  test) reduced levels of KNL1-pMELT in BCAT1-KO cells compared with control cells (Figure 4F), consistent with reduced TTK activity in BCAT1-KO cells.

### CXXC motif-dependent protein sulfenylation in mitotic cells

Cysteine-based redox switches regulate the activity of many kinases, phosphatases, and metabolic enzymes (Klomsiri et al., 2011; Lennicke and Cochem, 2021). BCAT1 contains a CXXC amino acid motif, whose oxidation reduces BCAT1 transaminase activity by about 50% (Conway et al., 2008). In addition, this CXXC redox switch was proposed to mediate thiol-disulfide oxidoreductase activity, suggesting BCAT1 could function as a redox chaperone or in redox signaling (El Hindy et al., 2014). To test whether BCAT1 affects the redox balance in cancer cells, we quantified cellular ROS in BCAT1-KO and control cells in response to ROS challenge. Upon treatment with 100 and 500  $\mu$ M hydrogen peroxide, we observed higher increases of ROS levels in BCAT1 KO than control cells (Figure 5A), suggesting that BCAT1 affects ROS balance.

Recently, Michael Yaffe and colleagues reported intracellular ROS and protein oxidation to increase as cells progress through the cell cycle, peaking in mitotic cells (Lim et al., 2020; Patterson et al., 2019). To address whether BCAT1-KO could affect protein oxidation, we labeled sulfenic acids (S-OH) in unsynchronized cancer cells with the clickable dimedone-derivative DYn-2 (Paulsen et al., 2011). Analysis of cells at different phases of the cell cycle, defined by DNA content and pH3 mitosis marker staining (Figure 5B), showed increasing thiol sulfenylation throughout cell cycle progression. However, in M phase, cysteine oxidation was significantly ( $p = 0.0163$ , two-sided  $t$  test) higher in BCAT1-KO than control cells (Figure 5C). In addition, to verify that BCAT1 KO results in the increased oxidation of mitotic regulator proteins, we analyzed the level of PP1 sulfenylation. PP1 counteracts mitotic kinases, including CDK1, and is essential for mitotic exit (Grallert et al., 2015; Holder et al., 2019). Furthermore, its activity is sensitive to cysteine oxidation (Singh et al., 2018). To detect PP1 sulfenylation, we first labeled sulfenic acids with DYn-2 in mitotic cells, immunoprecipitated PP1, and then we

### Figure 3. BCAT1 is essential for tumor cell division *in situ* and *in vivo*

- (A) Example immunofluorescence image of GLICO, showing GFP-expressing LN229 (LN229-GFP) cells growing within a mature organoid. The organization of mature organoids was confirmed by staining against the neuronal marker TUBB3 and the stem cell marker, SOX2.
- (B) Strategy to visualize individual cells undergoing cell division. Scale bar represents 50  $\mu$ m. Insets show GFP-positive mitotic tumor cell within organoid; scale bar represents 10  $\mu$ m.
- (C) Representative time-lapses of control and BCAT1-KO LN229 cells undergoing cell division within the organoid. Cells were selected as described in (B). White arrows point to missegregated chromosomes in BCAT1-KO cell.
- (D) Frequency of types of mitosis observed in control and BCAT1-KO LN229 cells imaged in the GLICO. Bars are mean values  $\pm$  SEM. Three organoids per condition were used (each organoid was considered as a biological replicate). Control,  $n = 27$  cells; BCAT1-KO  $n = 49$  cells.
- (E) Representative tumor *in vivo* images of the mice injected with luciferase-expressing mGB2 Control and BCAT1-KO cells 30 days after transplantation.
- (F) Control and BCAT1-KO tumor measurements from 30 to 100 days after mGB2 cell transplantation ( $n = 8$  mice per condition) expressed in total luminescence units.
- (G) Survival curve of the mice injected with Control and Bcat1-KO mGB2 cells ( $n = 8$  mice per condition). The significance of the survival difference ( $p = 0.0004$ ) between groups was calculated using log rank test with no censored events. The survival comparison was stopped at day 90 due to lack of obvious tumor formation in the Bcat1-KO-injected mice.
- (H) Representative tile scans of histological sections of mouse brains injected with mGB2 control or Bcat1-KO cells. Scale bar represents 500  $\mu$ m.
- (I) Mitotic cells were stained against pH3. Bcat1-expressing mGB2 tumors had a larger number of pH3-positive cells compared with Bcat1-KO mGB2 tumors. Scale bar represents 50  $\mu$ m.
- (J) Magnification into pH3-positive mGB2 cells showing normal mitosis in control cells and lagging chromosomes and anaphase bridges in Bcat1-KO cells. Scale bar represents 10  $\mu$ m. See also Figure S4 and Video S6.



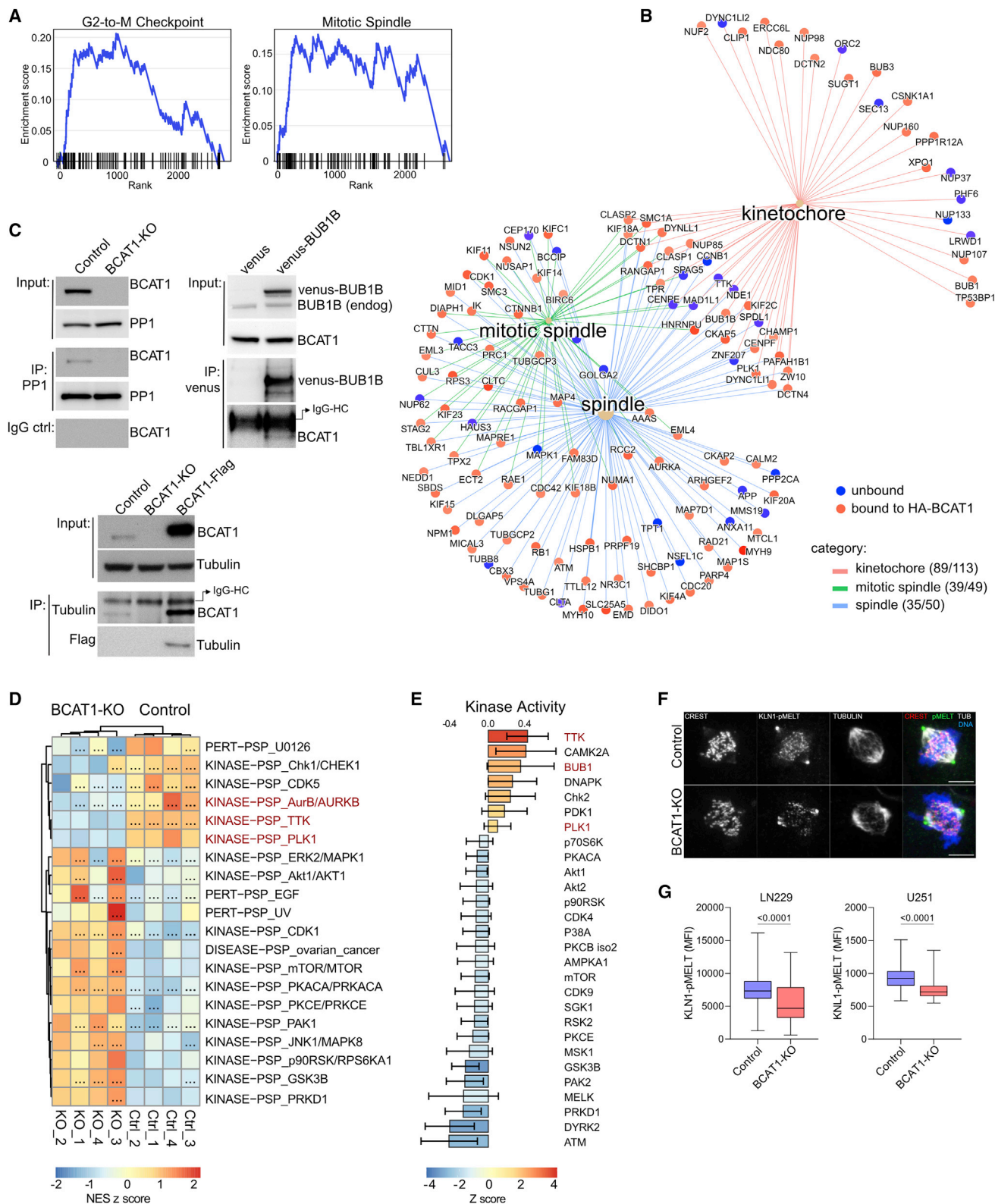


**Figure 4. BCAT1 interacts with and modulates SAC regulatory components**

(A) GSEA enrichment plots of G2-to-M Checkpoint and Mitotic Spindle signatures of HA-BCAT1-bound proteins. HA-BCAT1-bound proteins were ranked using the average log2 label-free quantification (LFQ) value ( $n = 3$ ) together with the unbound proteins identified in the input (assigned negative log2 LFQ values). The

(legend continued on next page)

performed Click-IT chemistry using Biotin-azide. Subsequent analysis of PP1 sulfenylation by Streptavidin-HRP western blotting revealed significantly ( $p = 0.0297$ , two-side  $t$  test) increased sulfenylation of PP1 in BCAT1-KO compared with control cells (Figures 5D and 5E). Together, these findings suggest an M-phase-specific control of cysteine oxidation by BCAT1.

To study how BCAT1 affects cysteine sulfenylation, we constructed BCAT1 functional mutants, i.e., catalytic-inactive BCAT1 in which we abolished transaminase activity through mutation of lysine 222 to alanine (BCAT1<sup>K222A</sup>), and a BCAT1 variant in which we mutated the cysteines 335 and 338 of the CXXC redox motif to serines (BCAT1<sup>SXXS</sup>). Analysis of the transaminase function of the BCAT1 variants *in vitro* confirmed the complete inactivation of the metabolic activity for BCAT1<sup>K222A</sup> and a reduction of about 50% for BCAT1<sup>SXXS</sup> (Figure 5F), consistent with previous reports (Conway et al., 2008). Next, we analyzed the phenotypic impact of the BCAT1 variants by expressing wild-type BCAT1 (BCAT1<sup>WT</sup>), BCAT1<sup>K222A</sup>, and BCAT1<sup>SXXS</sup> in LN229 BCAT1-KO cells (Figure 5G). Utilizing this knockout and rescue approach, we analyzed protein sulfenylation in nocodazole-synchronized mitotic cells. In agreement with our initial FACS-based analysis (Figure 5C), BCAT1-KO cells were significantly ( $p = 0.0382$ , one-way ANOVA) more oxidized than control cells. The expression of BCAT1<sup>WT</sup> ( $p = 0.0271$ , one-way ANOVA) and BCAT1<sup>K222A</sup> ( $p = 0.0421$ , one-way ANOVA) rescued this KO phenotype, while cells expressing BCAT1<sup>SXXS</sup> had cysteine oxidation levels not significantly different from BCAT1-KO cells (Figure 5H). These data indicate that the BCAT1 CXXC motif but not BCAT1 catalytic activity are required for BCAT1-mediated reduction of cysteine sulfenylation in mitotic cells.

Nevertheless, we additionally assessed potential effects on glutathione production since previous studies have pointed at the potential relevance of the BCAT-glutamate-glutathione axis in cancer (McBrayer et al., 2018; Wang et al., 2019). Analysis of total glutathione in nocodazole-synchronized cells showed a depletion by 32% in BCAT1-KO vs. control cells ( $p = 0.0007$ , one-way ANOVA), which was rescued by expression of BCAT1<sup>WT</sup> up to 86% of control levels ( $p = 0.0524$ , one-way ANOVA). On the contrary, glutathione levels remained unchanged in BCAT1-KO cells expressing the metabolic-dead mutant BCAT1<sup>K222A</sup> (Figure 5I). These data further support our conclusion that sulfenylation of mitotic proteins depends on

neither the metabolic transaminase activity of BCAT1 nor the total levels of intracellular glutathione.

In summary, these data indicate that the observed BCAT1-dependent reduction of protein sulfenylation in mitotic cells is mediated by a CXXC motif redox functionality.

### BCAT1 KO impairs inner-centromere localization of AURKB

Accurate chromosome segregation requires proper amphitelic kinetochore-microtubule attachments, involving an AURKB-controlled error correction mechanism at the SAC (Krenn and Musacchio, 2015; Lampson and Grishchuk, 2017). Therefore, we hypothesized that the decreased AURKB activity we inferred from phosphoproteomics analysis could contribute to the mitotic defects observed in BCAT1-KO cells. However, western blotting analysis showed no difference of pT232-AURKB activating phosphorylation between BCAT1-KO and control cells (Figure S6A). AURKB function requires its presence at the centromeres, which is regulated by KNL1-phosphorylation state (Faesen et al., 2017; Ji et al., 2017). Thus, we analyzed AURKB localization at the centromeric region in cells arrested at metaphase. Compared with their respective control cells, U251 and LN229 BCAT1-KO cells had a significantly decreased AURKB signals at centromeres (Figure S6B). Moreover, in U251 and LN229 BCAT1-KO vs. control cells, proper chromosome alignments at metaphase were significantly decreased (U251,  $p = 0.010$ ; LN229,  $p = 0.033$ ; two-sided  $t$  test), and severe misalignments involving six or more chromosomes significantly increased (U251,  $p = 0.025$ ; LN229,  $p = 0.028$ ; two-sided  $t$  test) (Figures S6C–S6E).

We then sought to study the dependency on the redox or the metabolic function of BCAT1 on AURKB localization and function. Reconstitution of BCAT1-KO cells with BCAT1<sup>WT</sup> resulted in a significant ( $p = 0.0434$ ; one-way ANOVA) rescue of AURKB localization at the centromere (Figure 6A). Likewise, cells expressing the metabolic-dead BCAT1<sup>K222A</sup> displayed a significant ( $p = 0.0068$ , one-way ANOVA) increased signal of AURKB at the centromere. This suggests that BCAT1-derived metabolites (including glutathione, see Figure 5I) are not determinants of AURKB localization. In contrast, cells expressing BCAT1<sup>SXXS</sup> displayed low signal of AURKB at the centromeres, mimicking BCAT1-KO cells. Consistent with these results, we observed a significant improvement of chromosome alignment at metaphases in both U251 and

ranked list was used to perform a pre-ranked GSEA analysis with the MSigDB Hallmark gene sets. The G2-to-M Checkpoint and Mitotic Spindle gene sets were found to be in the top 10 enriched signatures, with normalized enrichment scores (NES) of 2.3 and adjusted  $p$  values smaller than 0.01.

(B) Mitotic spindle and kinetochore protein networks extracted from Gene Ontology Cellular Compartment terms, where proteins that were found in HA-BCAT1 Co-IP are shown in red, and those found in the input but not bound to HA-BCAT1 are shown in blue.

(C) Co-IP confirming interaction of BCAT1 with the PP1, BUB1B, and tubulin.

(D) Z score NES heatmaps of 20 top differentially enriched pathways based on a site-specific phosphorylation analysis between mitotic Control (NT\_mito\_[1–4]) and BCAT1-KO (KO\_mito\_[1–4]) cells. Imputed vs.  $n$ -normalized LFQ values of each phospho-site per sample were used in an ssGSEA analysis with the PTMSigDB site-specific dataset. 20 pathways with the highest median NES difference between Control and BCAT1-KO samples are presented in the heatmap. “...” signifies significantly enriched signatures with a  $p$  value less than 0.05.

(E) Differential kinase activity analysis based on phospho-site-specific fold changes between mitotic Control and BCAT1-KO cells. Differentially phospho-sites were analyzed using the RoKAI R package. Normalized fold changes were compared with the PSP and Singor datasets with all available networks. Positive predicted kinase activity scores ( $x$  axis) and Z scores (color legend) refer to kinases that are more active in Control cells, whereas the negative scores describe kinases more active in BCAT1-KO cells.

(F) Representative images of U251 Control and BCAT1-KO cells arrested at metaphase and stained against CREST, KNL1-pMELT, and tubulin.

(G) Quantification of KNL1-pMELT (F) in LN229 and U251 showing decreased signal in BCAT1-KO cells compared with controls. More than 250 mitotic cells were quantified in at least three independent coverslips per condition.  $p$  values were determined by unpaired, two-sided  $t$  test. See also Figure S5.

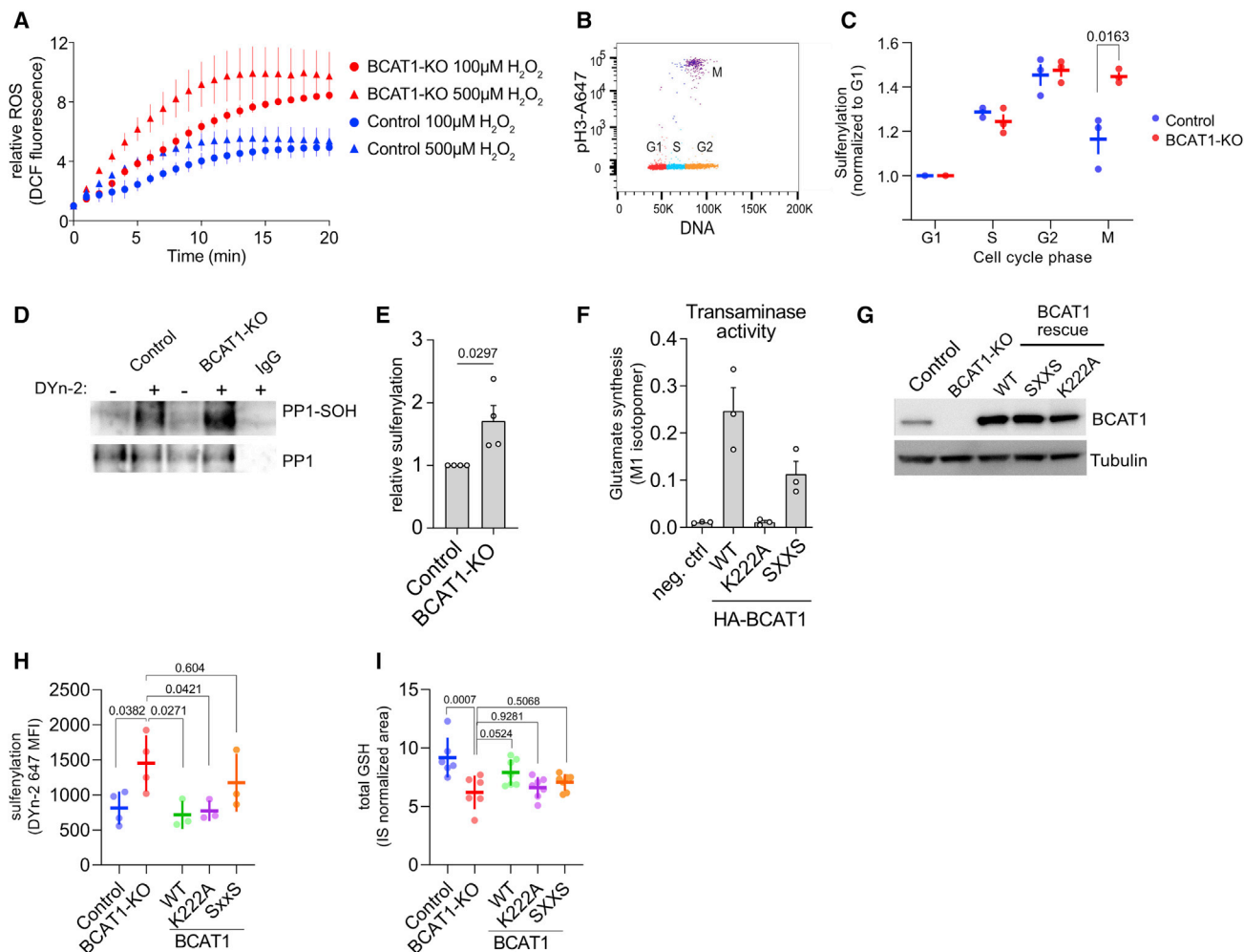


**Figure 5. BCAT1 regulates cellular redox balance in a metabolic-independent manner**

(A) ROS produced by U251 control or BCAT1-KO treated with 100 or 500  $\mu\text{M}$   $\text{H}_2\text{O}_2$ . Mean  $\pm$  SEM of three biological replicates. Intracellular ROS was determined using the fluorogenic dye DCFDA.

(B) Representative plot of flow cytometry analysis showing gating strategy. Cell cycle phases were detected using a combination of DNA staining and pH3.

(C) Quantification of mean fluorescence intensity (MFI) of unsynchronized cells labeled with DYN-2 measured at each cell cycle phase gated as shown in (A).  $n = 3$  biological replicates  $\pm$  SEM.

(D) Western blot showing sulfenylated PP1 in LN229 control and BCAT1-KO nocodazole-synchronized mitotic cells.

(E) Densitometric quantification of (D). Data were normalized to control of each experiment.  $n = 4$  biological replicates  $\pm$  SEM.

(F) *In vitro* transaminase assay of recombinant HA-BCAT1 mutants. WT = wild-type BCAT1, K222A = metabolic-dead mutant, SXXS = redox-dead mutant (C335S/C338S).

(G) Western blot showing comparable levels of expression of different BCAT1 mutants in LN229 BCAT1-KO cells. BCAT1 wild type (BCAT1<sup>WT</sup>), redox dead (BCAT1<sup>SXXS</sup>), or catalytic dead (BCAT1<sup>K222A</sup>).

(H) Sulfenylation levels (DYN-2 labeled) in cells synchronized with nocodazole and analyzed by flow cytometry. Cells were harvested by mitotic shake-off and labeled with 5mM DYN-2 for 30 min, followed by click-IT and pH3 staining; control and BCAT1-KO cells ( $n = 4$  biological replicates, each) and BCAT1-KO cells expressing the indicated BCAT1 mutants ( $n = 3$  biological replicates, each).

(I) Total cellular glutathione (GSH) levels in nocodazole-synchronized LN229 Control, BCAT1-KO, and BCAT1-KO expressing different BCAT1 mutants. In (E) and (F), bars represent mean values  $\pm$  SEM of at least three independent experiments. Data in panels (C), (H), and (I) are presented as mean (horizontal lines)  $\pm$  SD (vertical lines) of at least three biological replicates (dots). For (C) and (E), values were determined by unpaired, two-sided *t* test. For (H) and (I), the statistical significance was calculated using one-way ANOVA with Dunnett's multiple comparison test between BCAT1-KO cells and the indicated condition.

LN229 cells rescued with BCAT1<sup>WT</sup> and BCAT1<sup>K222A</sup>, but not in cells expressing BCAT1<sup>SXXS</sup> (Figures 6C, 6D, S6F, and S6G). Similar results were obtained after quantification of spindle and DNA symmetry traits in unsynchronized cells (Figures S6H and S6I).

### The BCAT1 CXXC redox motif is essential to maintain mitotic fidelity

Once shown that depletion of BCAT1 in glioblastoma cells causes downregulation of SAC and error correction signaling pathways (Figure 4) and that the absence of the BCAT1 redox-active CXXC



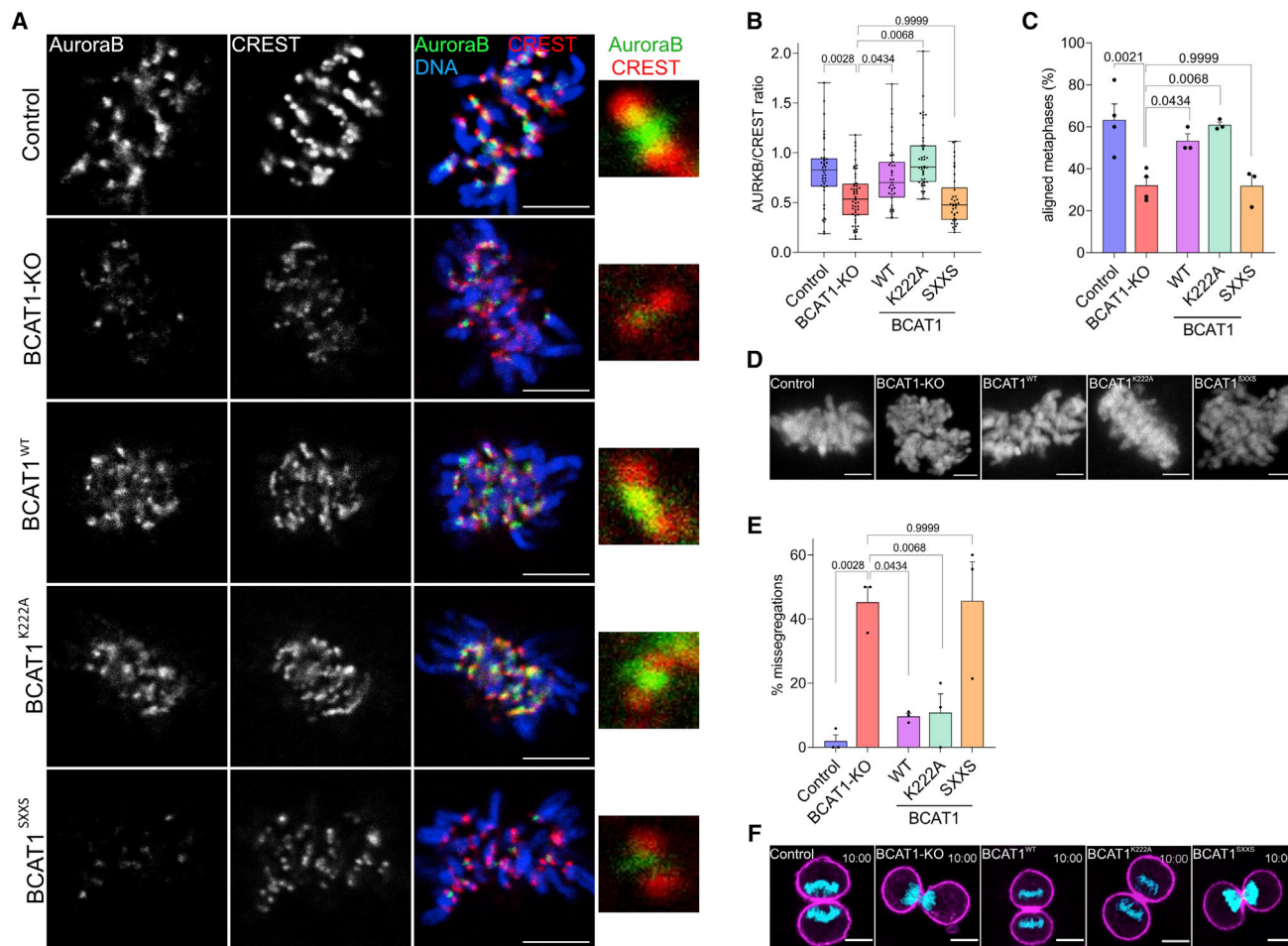


**Figure 6. CXXC motif of BCAT1 sustains AURKB localization and mitotic fidelity**

(A) Representative images of AURKB and CREST signals of the indicated cells. Magnification of representative kinetochores showing differential enrichment of AURKB in the indicated cell lines. Scale bars represent 10  $\mu$ m.

(B) MFI of AURKB normalized to CREST signal (AURKB/CREST) at the centromeres of the indicated cells. Dots indicate individual cells; control, n = 41; BCAT1-KO, n = 50; BCAT1<sup>WT</sup>, n = 39; BCAT1<sup>SXXS</sup>, n = 38; BCAT1<sup>K222A</sup>, n = 43.

(C) Percentage of imaged cells displaying aligned chromosomes at metaphase. Bars represent mean values  $\pm$  SEM of at least three independent experiments in which >12 cells were imaged per experiment. Control, n = 95; BCAT1-KO, n = 89; BCAT1<sup>WT</sup>, n = 40; BCAT1<sup>K222A</sup>, n = 42; BCAT1<sup>SXXS</sup>, n = 43. See also Figures S6C–S6G.

(D) Representative pictures of chromosome alignment of cells at metaphase. Scale bar represents 3  $\mu$ m.

(E) Percentage of cells that exhibit missegregated chromosomes. Bars represent mean values  $\pm$  SEM of three independent experiments. Control, n = 32; BCAT1-KO, n = 40; BCAT1<sup>WT</sup>, n = 32; BCAT1<sup>K222A</sup>, n = 33; BCAT1<sup>SXXS</sup>, n = 33.

(F) Representative images of cells of the mitotic outcomes of the different cell lines. LN229 control and cells expressing BCAT1<sup>WT</sup> and BCAT1<sup>K222A</sup> showed efficient segregation of chromosome, while in BCAT1-KO cells and cells expressing BCAT1<sup>SXXS</sup> experienced missegregations. Scale bar represents 5  $\mu$ m. See also Video S6. In panels (B), (C), and (D), the statistical significance was calculated using one-way ANOVA with Dunnett's multiple comparison test between BCAT1-KO cells and the indicated condition. Statistical analyses were carried out using GraphPad Prism 9.0.0 (San Diego, CA), and a p value < 0.05 was considered statistically significant.

motif reduced centromeric localization of AURKB and chromosome alignment, we questioned whether this redox function might also underlie the observed mitotic abnormalities. To answer this, we used live-cell imaging to analyze mitoses of BCAT1-KO cells with and without stable expression of BCAT1<sup>WT</sup> or the functional mutants BCAT1<sup>K222A</sup> or BCAT1<sup>SXXS</sup>. We found that 90.4% of cells expressing BCAT1<sup>WT</sup> and 89.2% of cells expressing BCAT1<sup>K222A</sup> were able to complete mitosis without observable missegregation, similar to control cells. In contrast, about 45.6% of cells expressing

BCAT1<sup>SXXS</sup> showed incomplete mitosis, which mimicked the phenotype observed in BCAT1-KO cells (Figures 6E and 6F and Video S6).

## DISCUSSION

The cell cycle is a highly complex process involving hundreds of proteins whose dysregulation is a common cause of cancer and other diseases (Heim et al., 2017; Matthews et al., 2021). Here,

we identified the metabolic enzyme BCAT1 as a mitotic regulator in both cancer and stem cells, underscoring its broad biological relevance.

Thiol-based redox signaling modulates the activity of kinases and phosphatases, effectively connecting ROS with cellular processes regulated by phospho-signaling, such as the cell cycle (Havens et al., 2006; Karisch et al., 2011; Leslie et al., 2003; Shao et al., 2014; Truong et al., 2016). However, the exact roles of ROS in mitosis remain poorly understood and sometimes appear conflicting (Burhans and Heintz, 2009; Menon and Goswami, 2007). Nonetheless, recent studies provide insights into the redox-mediated control of mitotic progression; i.e., PRDX1 was shown to shield centrosome-phosphatases from ROS-induced inactivation (Lim et al., 2015). Furthermore, analysis of actively cycling cancer cells indicated that the levels of ROS and biomolecule oxidation increase across the cell cycle (Patterson et al., 2019), resulting in sulfenylation of AURKA at C290, followed by disulfide-mediated AURKA dimerization and activation through T288 autophosphorylation at the onset of mitosis (Byrne et al., 2020; Lim et al., 2020; Tsuchiya et al., 2020).

Our data indicate that protein sulfenylation levels in mitotic cells are controlled by BCAT1 through its CXXC redox motif. Furthermore, we provide evidence for BCAT1-CXXC protecting cells against peroxide challenge, consistent with a recent study showing BCAT1 can metabolize hydrogen peroxide *in vitro* (Hillier et al., 2022). IP-MS and Co-IP analyses identified interactions of BCAT1 with the majority of proteins associated with the kinetochore and spindle. BCAT1-KO resulted in increased sulfenylation of total cellular protein and reduced activities of mitotic kinases, including the SAC regulator TTK (Pachis and Kops, 2018) and AURKB. These results link BCAT1 and its CXXC redox motif to the regulation of chromosome segregation by phosphorylation signaling.

AURKB is essential for correcting errors in kinetochore-microtubule attachment and ensuring accurate chromosome segregation. This function requires AURKB centromeric localization and activation by autophosphorylation (Lampson and Grishchuk, 2017). AURKB is structurally similar to AURKA, including the T288 (T232 in AURKB) autophosphorylation site and the C290 (C234 in AURKB) required for AURKA disulfide-mediated dimerization. Assuming an analogous mechanism regulating AURKB activity, we analyzed AURKB T232 phosphorylation and AURKB cellular localization. We detected no difference in T232 phosphorylation between BCAT1-KO and control cells, but AURKB failed to localize to centromeres in BCAT1-KO cells and BCAT1-KO cells expressing redox mutant BCAT1<sup>SXXS</sup>. These findings associate reduced AURKB activity in BCAT1-KO cells with aberrant AURKB localization.

Consistent with this hypothesis, we additionally inferred reduced activities of TTK and other kinases in BCAT1 KO cells from phosphoproteomics data, and we independently confirmed the loss of TTK activity by immunofluorescence analysis of KNL1 MELT repeat phosphorylation. KNL1-pMELT generates docking sites for the recruitment of BUB1, BUB3, and BUB1B, and it is essential for activation of the SAC and error correction mechanisms (Manic et al., 2017; Vleugel et al., 2015; Zhang et al., 2014). Whether TTK acts upstream or downstream of AURKB to regulate the SAC and error correction is controversial (Jelluma

et al., 2008; Saurin et al., 2011; van der Waal et al., 2012), but it is clear that their coordinated activities promote AURKB centromeric recruitment. Hence, we hypothesize that reduced TTK activity could also contribute to AURKB de-localization in BCAT1-KO cells and link the chromosome segregation defects and the increased cysteine oxidation observed in mitotic BCAT1-KO cells. No direct evidence for redox regulation of TTK has emerged so far; however, TTK is a potential binding partner of thioredoxin (Weingarten, 2008) and PRDX2 (Tobias Dick, personal communication), and TTK cysteines are oxidized during physiological aging (Xiao et al., 2020).

In conclusion, this study shows through a series of knockout and rescue experiments that BCAT1 has a non-metabolic function as a mitotic regulator facilitated through its redox motif. We showed mitotic abnormalities due to BCAT1 depletion to persist in glioma cerebral organoid and syngeneic mouse models, severely impacting tumor growth. The findings presented here suggest a possible explanation for the well-established role of BCAT1 in promoting cancer cell proliferation and provide a mechanistic framework for the development of therapies for BCAT1-dependent cancers.

### Limitations of the study

Here we show that BCAT1 affects total levels of cysteine oxidation in a cell-cycle-dependent manner. Future studies should focus in identifying protein-specific sulfenylation in a whole proteome level. Unfortunately, current methods for identification of residue-specific redox modifications typically require extremely large amounts of biologic material, limiting what can be done in highly dynamic cellular processes, such as mitosis, with currently available protocols. We also were not able to study morphological features and the localization of BCAT1 in our mouse model since mitotic structures cannot be preserved in fixed tissues. In addition, the separation of function mutants will have to be tested in mouse tumor models to directly support the essential role of the CXXC motif for *in vivo* tumor growth.

### STAR★METHODS

Detailed methods are provided in the online version of this paper and include the following:

- **KEY RESOURCES TABLE**
- **RESOURCE AVAILABILITY**
  - Lead contact
  - Materials availability
  - Data and code availability
- **EXPERIMENTAL MODEL AND SUBJECT DETAILS**
  - Cell lines and culture conditions
  - Mouse glioblastoma model
  - GLICO model and organoid culturing
- **METHOD DETAILS**
  - Generation of BCAT1 constructs
  - Lentiviral production
  - Generation of CRISPR/Cas9 knockout cell lines
  - Immunofluorescence
  - Live cell imaging
  - Click-iT™ EdU cell proliferation assay

- Tissue preparation
- Synchronization of cells in mitosis
- KNL1-pMELT, AURKB localization and chromosome alignment assays
- Co-immunoprecipitation and MS
- Phosphoproteomics
- DYn-2 labeling for detection of sulfenic acids
- HA-BCAT1 overexpression and purification for *in vitro* transaminase assays
- *In vitro* BCAT1 transaminase assay
- Determination of glutathione
- LC-MS analysis
- SDS-PAGE and western blot
- Transwell cell migration assay
- *In situ* brain slice invasion assay
- **QUANTIFICATION AND STATISTICAL ANALYSIS**

## SUPPLEMENTAL INFORMATION

Supplemental information can be found online at <https://doi.org/10.1016/j.celrep.2022.111524>.

## ACKNOWLEDGMENTS

The authors thank Prof. Conway for providing the BCAT1 antibody. We thank J.P.L. Kops for providing the KNL1-pMELT antibody. We would like to acknowledge Theresa Schmid, Matthias Plessner, Elisa Heinzemann, Anne Jenseit, and the DKFZ Microscopy and Proteomics Core Facilities for technical support. This work was supported by Deutsche Forschungsgemeinschaft grant GR 2111/10-1 to R.G. in the context of the German Excellence Strategy (EXC-2189, project ID 390939984).

## AUTHOR CONTRIBUTIONS

L.F. designed the study, performed and analyzed the majority of experiments, and wrote the manuscript. P.B. performed animal experiments and analyzed proteomics data. J.K. and C.S. performed and analyzed live-cell imaging experiments. W.H., T.H.M., and M.S. performed cellular and biochemical assays. K.H., R.G., and P.L. provided logistic and financial support. B.R. designed and supervised the study and wrote the manuscript.

## DECLARATION OF INTERESTS

The authors declare no competing interests.

Received: March 7, 2021

Revised: August 15, 2022

Accepted: September 26, 2022

Published: October 18, 2022

## REFERENCES

Ananieva, E.A., and Wilkinson, A.C. (2018). Branched-chain amino acid metabolism in cancer. *Curr. Opin. Clin. Nutr. Metab. Care* 21, 64–70. <https://doi.org/10.1097/MCO.0000000000000430>.

Battello, N., Zimmer, A.D., Goebel, C., Dong, X., Behrmann, I., Haan, C., Hiller, K., and Wegner, A. (2016). The role of HIF-1 in oncostatin M-dependent metabolic reprogramming of hepatic cells. *Cancer Metab.* 4, 3. <https://doi.org/10.1186/s40170-016-0141-0>.

Burhans, W.C., and Heintz, N.H. (2009). The cell cycle is a redox cycle. linking phase-specific targets to cell fate. *Free Radic. Biol. Med.* 47, 1282–1293. <https://doi.org/10.1016/j.freeradbiomed.2009.05.026>.

Byrne, D.P., Shrestha, S., Galler, M., Cao, M., Daly, L.A., Campbell, A.E., Evers, C.E., Veal, E.A., Kannan, N., and Evers, P.A. (2020). Aurora A regulation by reversible cysteine oxidation reveals evolutionarily conserved redox control of Ser/Thr protein kinase activity. *Sci. Signal.* 13, eaax2713. <https://doi.org/10.1126/scisignal.aax2713>.

Coles, S.J., Hancock, J.T., and Conway, M.E. (2012). Differential redox potential between the human cytosolic and mitochondrial branched-chain aminotransferase. *Acta Biochim. Biophys. Sin.* 44, 172–176. <https://doi.org/10.1093/abbs/gmr103>.

Conway, M.E. (2020). Emerging moonlighting functions of the branched-chain aminotransferase (BCAT) proteins. *Antioxid. Redox Signal* 34, 1048–1067. <https://doi.org/10.1089/ars.2020.8118>.

Conway, M.E., Coles, S.J., Islam, M.M., and Hutson, S.M. (2008). Regulatory control of human cytosolic branched-chain aminotransferase by oxidation and S-glutathionylation and its interactions with redox sensitive neuronal proteins. *Biochemistry* 47, 5465–5479. <https://doi.org/10.1021/bi800303h>.

Costa, B., Fletcher, M.N.C., Boskovic, P., Ivanova, E.L., Eisemann, T., Lohr, S., Bunse, L., Löwer, M., Burchard, S., Korshunov, A., et al. (2021). A set of cell lines derived from a genetic murine glioblastoma model recapitulates molecular and morphological characteristics of human tumors. *Cancers* 13, E230. <https://doi.org/10.3390/cancers13020230>.

Cox, J., Hein, M.Y., Luber, C.A., Paron, I., Nagaraj, N., and Mann, M. (2014). Accurate proteome-wide label-free quantification by delayed normalization and maximal peptide ratio extraction, termed MaxLFQ. *Mol. Cell. Proteomics* 13, 2513–2526.

de Bont, J.M., Kros, J.M., Passier, M.M.C.J., Reddingius, R.E., Sillevius Smitt, P.A.E., Luiders, T.M., den Boer, M.L., and Pieters, R. (2008). Differential expression and prognostic significance of SOX genes in pediatric medulloblastoma and ependymoma identified by microarray analysis. *Neuro. Oncol.* 10, 648–660. <https://doi.org/10.1215/15228517-2008-032>.

Eisemann, T., Costa, B., Strelau, J., Mittelbronn, M., Angel, P., and Peterziel, H. (2018). An advanced glioma cell invasion assay based on organotypic brain slice cultures. *BMC Cancer* 18, 103. <https://doi.org/10.1186/s12885-018-4007-4>.

El Hindy, M., Hezwani, M., Corry, D., Hull, J., El Amraoui, F., Harris, M., Lee, C., Forshaw, T., Wilson, A., Mansbridge, A., et al. (2014). The branched-chain aminotransferase proteins: novel redox chaperones for protein disulfide isomerase—implications in Alzheimer's disease. *Antioxid. Redox Signal* 20, 2497–2513. <https://doi.org/10.1089/ars.2012.4869>.

Faesen, A.C., Thanasoulas, M., Maffini, S., Breit, C., Müller, F., van Gerwen, S., Bange, T., and Musacchio, A. (2017). Basis of catalytic assembly of the mitotic checkpoint complex. *Nature* 542, 498–502. <https://doi.org/10.1038/nature21384>.

García-Espinosa, M.A., Wallin, R., Hutson, S.M., and Sweatt, A.J. (2007). Widespread neuronal expression of branched-chain aminotransferase in the CNS: implications for leucine/glutamate metabolism and for signaling by amino acids. *J. Neurochem.* 100, 1458–1468. <https://doi.org/10.1111/j.1471-4159.2006.04332.x>.

Grallert, A., Boke, E., Hagting, A., Hodgson, B., Connolly, Y., Griffiths, J.R., Smith, D.L., Pines, J., and Hagan, I.M. (2015). A PP1-PP2A phosphatase relay controls mitotic progression. *Nature* 517, 94–98. <https://doi.org/10.1038/nature14019>.

Gu, Z., Liu, Y., Cai, F., Patrick, M., Zmajkovic, J., Cao, H., Zhang, Y., Tasdogan, A., Chen, M., Qi, L., et al. (2019). Loss of EZH2 reprograms BCAA metabolism to drive leukemic transformation. *Cancer Discov.* 9, 1228–1247. <https://doi.org/10.1158/2159-8290.CD-19-0152>.

Häfner, J., Mayr, M.I., Möckel, M.M., and Mayer, T.U. (2014). Pre-anaphase chromosome oscillations are regulated by the antagonistic activities of Cdk1 and PP1 on Kif18A. *Nat. Commun.* 5, 4397. <https://doi.org/10.1038/ncomms5397>.

Hanschmann, E.M., Godoy, J.R., Berndt, C., Hudemann, C., and Lillig, C.H. (2013). Thioredoxins, glutaredoxins, and peroxiredoxins—molecular mechanisms and health significance: from cofactors to antioxidants to redox



- p>signaling.
- Antioxid. Redox Signal.*
- 19**
- , 1539–1605.
- <https://doi.org/10.1089/ars.2012.4599>
- .
- Hattori, A., Tsunoda, M., Konuma, T., Kobayashi, M., Nagy, T., Glushka, J., Tayyari, F., McSkimming, D., Kannan, N., Tojo, A., et al. (2017). Cancer progression by reprogrammed BCAA metabolism in myeloid leukaemia. *Nature* **545**, 500–504. <https://doi.org/10.1038/nature22314>.
- Havens, C.G., Ho, A., Yoshioka, N., and Dowdy, S.F. (2006). Regulation of late G1/S phase transition and APC Cdh1 by reactive oxygen species. *Mol. Cell Biol.* **26**, 4701–4711. <https://doi.org/10.1128/mcb.00303-06>.
- Hayes, J.D., Dinkova-Kostova, A.T., and Tew, K.D. (2020). Oxidative stress in cancer. *Cancer Cell* **38**, 167–197. <https://doi.org/10.1016/j.ccell.2020.06.001>.
- Heim, A., Rymarczyk, B., and Mayer, T.U. (2017). Regulation of cell division. In *Vertebrate Development. Maternal to Zygotic Control*, F. Pelegri, M. Danilchik, and A. Sutherland, eds. (Springer International Publishing), pp. 83–116. [https://doi.org/10.1007/978-3-319-46095-6\\_3](https://doi.org/10.1007/978-3-319-46095-6_3).
- Hiller, K., Hangebrauk, J., Jäger, C., Spura, J., Schreiber, K., and Schomburg, D. (2009). MetaboliteDetector. comprehensive analysis tool for targeted and nontargeted GC/MS based metabolome analysis. *Anal. Chem.* **81**, 3429–3439. <https://doi.org/10.1021/ac802689c>.
- Hillier, J., Allcott, G.J., Guest, L.A., Heaselgrave, W., Tonks, A., Conway, M.E., Cherry, A.L., and Coles, S.J. (2022). The BCAT1 CXXC motif provides protection against ROS in acute myeloid leukaemia cells. *Antioxidants* **11**, 683. <https://doi.org/10.3390/antiox11040683>.
- Holder, J., Poser, E., and Barr, F.A. (2019). Getting out of mitosis. spatial and temporal control of mitotic exit and cytokinesis by PP1 and PP2A. *FEBS Lett.* **593**, 2908–2924. <https://doi.org/10.1002/1873-3468.13595>.
- Hutson, S.M., Sweatt, A.J., and Lanoue, K.F. (2005). Branched-chain [corrected] amino acid metabolism. implications for establishing safe intakes. *J. Nutr.* **135**, 1557S–1564S. <https://doi.org/10.1093/jn/135.6.1557S>.
- Ichihara, A., and Koyama, E. (1966). Transaminase of branched chain amino acids. I. Branched chain amino acids- $\alpha$ -ketoglutarate transaminase. *J. Biochem.* **59**, 160–169. <https://doi.org/10.1093/oxfordjournals.jbchem.a128277>.
- Jelluma, N., Brenkman, A.B., van den Broek, N.J.F., Crujisen, C.W.A., van Osch, M.H.J., Lens, S.M.A., Medema, R.H., and Kops, G.J.P.L. (2008). Mps1 phosphorylates Borealin to control Aurora B activity and chromosome alignment. *Cell* **132**, 233–246. <https://doi.org/10.1016/j.cell.2007.11.046>.
- Ji, Z., Gao, H., Jia, L., Li, B., and Yu, H. (2017). A sequential multi-target Mps1 phosphorylation cascade promotes spindle checkpoint signaling. *Elife* **6**, e22513. <https://doi.org/10.7554/eLife.22513>.
- Karisch, R., Fernandez, M., Taylor, P., Virtanen, C., St-Germain, J.R., Jin, L.L., Harris, I.S., Mori, J., Mak, T.W., Senis, Y.A., et al. (2011). Global proteomic assessment of the classical protein-tyrosine phosphatome and “Redoxome”. *Cell* **146**, 826–840. <https://doi.org/10.1016/j.cell.2011.07.020>.
- Kim, H.J., Kim, T., Hoffman, N.J., Xiao, D., James, D.E., Humphrey, S.J., and Yang, P. (2021). PhosR enables processing and functional analysis of phosphoproteomic data. *Cell Rep.* **34**, 108771. <https://doi.org/10.1016/j.celrep.2021.108771>.
- Kirova, D.G., Judasova, K., Vorhauser, J., Zerjatke, T., Leung, J.K., Glauche, I., and Mansfeld, J. (2022). A ROS-dependent mechanism promotes CDK2 phosphorylation to drive progression through S phase. *Dev. Cell* **57**, 1712–1727.e9. <https://doi.org/10.1016/j.devcel.2022.06.008>.
- Klomsiri, C., Karplus, P.A., and Poole, L.B. (2011). Cysteine-based redox switches in enzymes. *Antioxid. Redox Signal.* **14**, 1065–1077. <https://doi.org/10.1089/ars.2010.3376>.
- Krenn, V., and Musacchio, A. (2015). The Aurora B kinase in chromosome bi-orientation and spindle checkpoint signaling. *Front. Oncol.* **5**, 225. <https://doi.org/10.3389/fonc.2015.00225>.
- Krug, K., Mertins, P., Zhang, B., Hornbeck, P., Raju, R., Ahmad, R., Szucs, M., Mundt, F., Forestier, D., Jane-Valbuena, J., et al. (2019). A curated resource for phosphosite-specific signature analysis. *Mol. Cell. Proteomics* **18**, 576–593. <https://doi.org/10.1074/mcp.TIR118.000943>.
- Lampson, M.A., and Grishchuk, E.L. (2017). Mechanisms to avoid and correct erroneous kinetochore-microtubule attachments. *Biology* **6**, E1. <https://doi.org/10.3390/biology6010001>.
- Lancaster, O.M., and Baum, B. (2014). Shaping up to divide. coordinating actin and microtubule cytoskeletal remodelling during mitosis. *Semin. Cell Dev. Biol.* **34**, 109–115. <https://doi.org/10.1016/j.semcdb.2014.02.015>.
- Lancaster, M.A., and Knoblich, J.A. (2014). Generation of cerebral organoids from human pluripotent stem cells. *Nat. Protoc.* **9**, 2329–2340. <https://doi.org/10.1038/nprot.2014.158>.
- Lenicke, C., and Cochemé, H.M. (2021). Redox metabolism. ROS as specific molecular regulators of cell signaling and function. *Mol. Cell* **81**, 3691–3707. <https://doi.org/10.1016/j.molcel.2021.08.018>.
- Leslie, N.R., Bennett, D., Lindsay, Y.E., Stewart, H., Gray, A., and Downes, C.P. (2003). Redox regulation of PI 3-kinase signalling via inactivation of PTEN. *EMBO J.* **22**, 5501–5510. <https://doi.org/10.1093/emboj/cdg513>.
- Lillig, C.H., Berndt, C., and Holmgren, A. (2008). Glutaredoxin systems. *Biochim. Biophys. Acta* **1780**, 1304–1317. <https://doi.org/10.1016/j.bbagen.2008.06.003>.
- Lim, D.C., Joukov, V., Rettenmaier, T.J., Kumagai, A., Dunphy, W.G., Wells, J.A., and Yaffe, M.B. (2020). Redox priming promotes Aurora A activation during mitosis. *Sci. Signal.* **13**, eabb6707. <https://doi.org/10.1126/scisignal.abb6707>.
- Lim, J.M., Lee, K.S., Woo, H.A., Kang, D., and Rhee, S.G. (2015). Control of the pericentrosomal H2O2 level by peroxiredoxin I is critical for mitotic progression. *J. Cell Biol.* **210**, 23–33. <https://doi.org/10.1083/jcb.201412068>.
- Linkous, A., Balamatsias, D., Snuderl, M., Edwards, L., Miyaguchi, K., Milner, T., Reich, B., Cohen-Gould, L., Storaska, A., Nakayama, Y., et al. (2019). Modeling patient-derived glioblastoma with cerebral organoids. *Cell Rep.* **26**, 3203–3211.e5. <https://doi.org/10.1016/j.celrep.2019.02.063>.
- Manic, G., Corradi, F., Sistigu, A., Siteni, S., and Vitale, I. (2017). Molecular regulation of the spindle assembly checkpoint by kinases and phosphatases. *Int. Rev. Cell Mol. Biol.* **328**, 105–161. <https://doi.org/10.1016/bs.ircmb.2016.08.004>.
- Matthews, H.K., Bertoli, C., and de Bruin, R.A.M. (2021). Cell cycle control in cancer. *Nat. Rev. Mol. Cell Biol.* **23**, 74–88. <https://doi.org/10.1038/s41580-021-00404-3>.
- Mayers, J.R., Torrence, M.E., Danai, L.V., Papagiannakopoulos, T., Davidson, S.M., Bauer, M.R., Lau, A.N., Ji, B.W., Dixit, P.D., Hosios, A.M., et al. (2016). Tissue of origin dictates branched-chain amino acid metabolism in mutant Kras-driven cancers. *Science* **353**, 1161–1165. <https://doi.org/10.1126/science.aaf5171>.
- McBrayer, S.K., Mayers, J.R., DiNatale, G.J., Shi, D.D., Khanal, J., Chakraborty, A.A., Sarosiek, K.A., Briggs, K.J., Robbins, A.K., Sevastianik, T., et al. (2018). Transaminase inhibition by 2-hydroxyglutarate impairs glutamate biosynthesis and redox homeostasis in glioma. *Cell* **175**, 101–116.e25. <https://doi.org/10.1016/j.cell.2018.08.038>.
- Menon, S.G., and Goswami, P.C. (2007). A redox cycle within the cell cycle. ring in the old with the new. *Oncogene* **26**, 1101–1109. <https://doi.org/10.1038/sj.onc.1209895>.
- Pachis, S.T., and Kops, G.J.P.L. (2018). Leader of the SAC. molecular mechanisms of Mps1/TTK regulation in mitosis. *Open Biol.* **8**, 180109. <https://doi.org/10.1098/rsob.180109>.
- Patterson, J.C., Joughin, B.A., van de Kooij, B., Lim, D.C., Lauffenburger, D.A., and Yaffe, M.B. (2019). ROS and oxidative stress are elevated in mitosis during asynchronous cell cycle progression and are exacerbated by mitotic arrest. *Cell Syst.* **8**, 163–167.e2. <https://doi.org/10.1016/j.cels.2019.01.005>.
- Paulsen, C.E., Truong, T.H., Garcia, F.J., Homann, A., Gupta, V., Leonard, S.E., and Carroll, K.S. (2011). Peroxide-dependent sulfenylation of the EGFR catalytic site enhances kinase activity. *Nat. Chem. Biol.* **8**, 57–64. <https://doi.org/10.1038/nchembio.736>.
- Raffel, S., Falcone, M., Kneisel, N., Hansson, J., Wang, W., Lutz, C., Bullinger, L., Poschet, G., Nonnenmacher, Y., Barnert, A., et al. (2017). BCAT1 restricts

alphaKG levels in AML stem cells leading to IDHmut-like DNA hypermethylation. *Nature* 551, 384–388. <https://doi.org/10.1038/nature24294>.

Ran, F.A., Hsu, P.D., Wright, J., Agarwala, V., Scott, D.A., and Zhang, F. (2013). Genome engineering using the CRISPR-Cas9 system. *Nat. Protoc.* 8, 2281–2308. <https://doi.org/10.1038/nprot.2013.143>.

Sanjana, N.E., Shalem, O., and Zhang, F. (2014). Improved vectors and genome-wide libraries for CRISPR screening. *Nat. Methods* 11, 783–784. <https://doi.org/10.1038/nmeth.3047>.

Saurin, A.T., van der Waal, M.S., Medema, R.H., Lens, S.M.A., and Kops, G.J.P.L. (2011). Aurora B potentiates Mps1 activation to ensure rapid checkpoint establishment at the onset of mitosis. *Nat. Commun.* 2, 316. <https://doi.org/10.1038/ncomms1319>.

Shao, D., Oka, S.I., Liu, T., Zhai, P., Ago, T., Sciarretta, S., Li, H., and Sadoshima, J. (2014). A redox-dependent mechanism for regulation of AMPK activation by Thioredoxin1 during energy starvation. *Cell Metab.* 19, 232–245. <https://doi.org/10.1016/j.cmet.2013.12.013>.

Sies, H., and Jones, D.P. (2020). Reactive oxygen species (ROS) as pleiotropic physiological signalling agents. *Nat. Rev. Mol. Cell Biol.* 21, 363–383. <https://doi.org/10.1038/s41580-020-0230-3>.

Silva, L.S., Poschet, G., Nonnenmacher, Y., Becker, H.M., Sapcaru, S., Gaupel, A.C., Schlotter, M., Wu, Y., Kneisel, N., Seiffert, M., et al. (2017). Branched-chain ketoacids secreted by glioblastoma cells via MCT1 modulate macrophage phenotype. *EMBO Rep.* 18, 2172–2185. <https://doi.org/10.15252/embr.201744154>.

Singh, S., Lmmle, S., Giese, H., Kmmmerer, S., Meyer-roxla, S., Alfari, E.A., Dihazi, H., Guan, K., El-armouche, A., and Richter, F. (2018). The reduced activity of PP-1 $\alpha$  under redox stress condition is a consequence of GSH-mediated transient disulfide formation. *Sci. Rep.* 8, 17711. <https://doi.org/10.1038/s41598-018-36267-6>.

Sivanand, S., and Vander Heiden, M.G. (2020). Emerging roles for branched-chain amino acid metabolism in cancer. *Cancer Cell* 37, 147–156. <https://doi.org/10.1016/j.ccell.2019.12.011>.

Smith, R.J., Cordeiro, M.H., Davey, N.E., Vallardi, G., Ciliberto, A., Gross, F., and Saurin, A.T. (2019). PP1 and PP2A use opposite phospho-dependencies to control distinct processes at the kinetochore. *Cell Rep.* 28, 2206–2219.e8. <https://doi.org/10.1016/j.celrep.2019.07.067>.

Su, K.C., Barry, Z., Schweizer, N., Maiato, H., Bathe, M., and Cheeseman, I.M. (2016). A regulatory switch alters chromosome motions at the metaphase-to-anaphase transition. *Cell Rep.* 17, 1728–1738. <https://doi.org/10.1016/j.celrep.2016.10.046>.

Sweatt, A.J., Wood, M., Suryawan, A., Wallin, R., Willingham, M.C., and Hutson, S.M. (2004). Branched-chain amino acid catabolism: unique segregation of pathway enzymes in organ systems and peripheral nerves. *Am. J. Physiol. Endocrinol. Metab.* 286, E64–E76. <https://doi.org/10.1152/ajpendo.00276.2003>.

Taylor, R.T., and Jenkins, W.T. (1966). Leucine aminotransferase. II. Purification and characterization. *J. Biol. Chem.* 241, 4396–4405.

Thewes, V., Simon, R., Hlevnjak, M., Schlotter, M., Schroeter, P., Schmidt, K., Wu, Y., Anzeneder, T., Wang, W., Windisch, P., et al. (2017). The branched-chain amino acid transaminase 1 sustains growth of antiestrogen-resistant and ERalpha-negative breast cancer. *Oncogene* 36, 4124–4134. <https://doi.org/10.1038/onc.2017.32>.

Tönjes, M., Barbus, S., Park, Y.J., Wang, W., Schlotter, M., Lindroth, A.M., Plier, S.V., Bai, A.H.C., Karra, D., Piro, R.M., et al. (2013). BCAT1 promotes cell proliferation through amino acid catabolism in gliomas carrying wild-type IDH1. *Nat. Med.* 19, 901–908. <https://doi.org/10.1038/nm.3217>.

Truong, T.H., Ung, P.M.U., Palde, P.B., Paulsen, C.E., Schlessinger, A., and Carroll, K.S. (2016). Molecular basis for redox activation of epidermal growth factor receptor kinase. *Cell Chem. Biol.* 23, 837–848. <https://doi.org/10.1016/j.chembiol.2016.05.017>.

Tsuchiya, Y., Byrne, D.P., Burgess, S.G., Bormann, J., Baković, J., Huang, Y., Zhyvoloup, A., Yu, B.Y.K., Peak-Chew, S., Tran, T., et al. (2020). Covalent Aurora A regulation by the metabolic integrator coenzyme A. *Redox Biol.* 28, 101318. <https://doi.org/10.1016/j.redox.2019.101318>.

van der Waal, M.S., Saurin, A.T., Vromans, M.J.M., Vleugel, M., Wurzenberger, C., Gerlich, D.W., Medema, R.H., Kops, G.J.P.L., and Lens, S.M.A. (2012). Mps1 promotes rapid centromere accumulation of Aurora B. *EMBO Rep.* 13, 847–854. <https://doi.org/10.1038/embor.2012.93>.

Vleugel, M., Omerzu, M., Groenewold, V., Hadders, M.A., Lens, S.M.A., and Kops, G.J.P.L. (2015). Sequential multisite phospho-regulation of KNL1-BUB3 interfaces at mitotic kinetochores. *Mol. Cell* 57, 824–835. <https://doi.org/10.1016/j.molcel.2014.12.036>.

Wang, Y., Zhang, J., Ren, S., Sun, D., Huang, H.Y., Wang, H., Jin, Y., Li, F., Zheng, C., Yang, L., et al. (2019). Branched-chain amino acid metabolic reprogramming orchestrates drug resistance to EGFR tyrosine kinase inhibitors. *Cell Rep.* 28, 512–525.e6. <https://doi.org/10.1016/j.celrep.2019.06.026>.

Weingarten, L. (2008). Identification of Novel Cytosolic Thioredoxin-1 Target Proteins in Mammalian Cells by Mechanism-Based Kinetic Trapping (Ru-precht-Karls University of Heidelberg).

Wiredja, D.D., Koyutürk, M., and Chance, M.R. (2017). The KSEA App: a web-based tool for kinase activity inference from quantitative phosphoproteomics. *Bioinformatics* 33, 3489–3491. <https://doi.org/10.1093/bioinformatics/btx415>.

Wu, J.Q., Guo, J.Y., Tang, W., Yang, C.S., Freel, C.D., Chen, C., Nairn, A.C., and Kornbluth, S. (2009). PP1-mediated dephosphorylation of phosphoproteins at mitotic exit is controlled by inhibitor-1 and PP1 phosphorylation. *Nat. Cell Biol.* 11, 644–651. <https://doi.org/10.1038/ncb1871>.

Xiao, H., Jedrychowski, M.P., Schweppe, D.K., Huttlin, E.L., Yu, Q., Heppner, D.E., Li, J., Long, J., Mills, E.L., Szpyt, J., et al. (2020). A quantitative tissue-specific landscape of protein redox regulation during aging. *Cell* 180, 968–983.e24. <https://doi.org/10.1016/j.cell.2020.02.012>.

Yılmaz, S., Ayati, M., Schlatter, D., Çiçek, A.E., Chance, M.R., and Koyutürk, M. (2021). Robust inference of kinase activity using functional networks. *Nat. Commun.* 12, 1177. <https://doi.org/10.1038/s41467-021-21211-6>.

Yoshikawa, R., Yanagi, H., Shen, C.S., Fujiwara, Y., Noda, M., Yagyu, T., Gega, M., Oshima, T., Yamamura, T., Okamura, H., et al. (2006). ECA39 is a novel distant metastasis-related biomarker in colorectal cancer. *World J. Gastroenterol.* 12, 5884–5889. <https://doi.org/10.3748/wjg.v12.i36.5884>.

Zhang, G., Lischetti, T., and Nilsson, J. (2014). A minimal number of MELT repeats supports all the functions of KNL1 in chromosome segregation. *J. Cell Sci.* 127, 871–884. <https://doi.org/10.1242/jcs.139725>.

Zhou, W., Feng, X., Ren, C., Jiang, X., Liu, W., Huang, W., Liu, Z., Li, Z., Zeng, L., Wang, L., et al. (2013). Over-expression of BCAT1, a c-Myc target gene, induces cell proliferation, migration and invasion in nasopharyngeal carcinoma. *Mol. Cancer* 12, 53. <https://doi.org/10.1186/1476-4598-12-53>.

Zhu, J., and Thompson, C.B. (2019). Metabolic regulation of cell growth and proliferation. *Nat. Rev. Mol. Cell Biol.* 20, 436–450. <https://doi.org/10.1038/s41580-019-0123-5>.

Zhu, Z., Achreja, A., Meurs, N., Animasahun, O., Owen, S., Mittal, A., Parikh, P., Lo, T.W., Franco-Barraza, J., Shi, J., et al. (2020). Tumour-reprogrammed stromal BCAT1 fuels branched-chain ketoacid dependency in stromal-rich PDAC tumours. *Nat. Metab.* 2, 775–792. <https://doi.org/10.1038/s42255-020-0226-5>.

## STAR★METHODS

### KEY RESOURCES TABLE

REAGENT or RESOURCE	SOURCE	IDENTIFIER
<b>Antibodies</b>		
mouse monoclonal anti-alpha Tubulin (DM1A)	Santa Cruz Biotechnology	Cat# sc-32293; RRID:AB_628412
mouse monoclonal anti-alpha Tubulin	Sigma-Aldrich	Cat# T9026; RRID:AB_477593
rabbit polyclonal anti-AuroraB/AIM1	Cell Signaling Technology	Cat# 3094; RRID:AB_10695307
rabbit polyclonal anti-BCAT1	Atlas Antibodies, Sigma-Aldrich	Cat# HPA048592; RRID:AB_2680454
Purified Mouse Anti-ECA39	BD Biosciences	Cat# 611271; RRID:AB_398799
rabbit antiserum against BCAT1	Prof. Myra Conway (UK)	N/A
rabbit polyclonal anti-Centrin-1	Abcam	Cat# ab11257; RRID:AB_2244666
human polyclonal anti-Centromere	Antibodies Incorporated	Cat# 15-234-0001; RRID:AB_2687472
rabbit polyclonal anti-SOX2	Millipore	Cat# AB5603; RRID:AB_2286686
Rabbit polyclonal anti-HA tag - ChIP Grade	Abcam	Cat# ab9110; RRID:AB_307019
Rabbit Anti-Histone H3, phospho (Ser10) Monoclonal Antibody, Unconjugated, Clone D2C8	Cell Signaling Technology	Cat# 3377; RRID:AB_1549592
mouse monoclonal anti-Tubulin beta 3 (TUBB3)	Biolegend	Cat# 801213; RRID:AB_2728521
Chicken polyclonal anti-GFP	Abcam	Cat# ab13970; RRID:AB_300798
rabbit anti-Ki67	Abcam	Cat# ab15580; RRID:AB_443209
Goat anti-Mouse IgG (H + L) Cross-Adsorbed Secondary Antibody, Alexa Fluor™ 488	Thermo Fisher Scientific	Cat# A-11001; RRID:AB_2534069
Goat anti-Rabbit IgG (H + L) Highly Cross-Adsorbed Secondary Antibody, Alexa Fluor™ 647	Thermo Fisher Scientific	Cat# A-21245; RRID:AB_2535813
anti-human Cy3	Abcam	Cat# ab97170; RRID: AB_10679896
PP1 Antibody (E-9)	Santa Cruz Biotechnology	Cat# sc-7482; RRID:AB_628177
PP1 alpha Polyclonal Antibody	Life Technologies	Cat# PA528218; RRID:AB_2545694
anti-KNL1 pT943/pT1155 (pMELT 23) AB	Geert J.P.L. Kops Lab (Netherlands)	N/A
Goat anti-Rabbit IgG (H + L) Highly Cross-Adsorbed Secondary Antibody, Alexa Fluor™ 488	Thermo Fisher Scientific	Cat# A-11034; RRID:AB_2576217
<b>Bacterial and virus strains</b>		
One Shot™ TOP10 Chemically Competent <i>E. coli</i>	Invitrogen™	C404010
One Shot™ Stbl3™ Chemically Competent <i>E. coli</i>	Invitrogen™	C737303
One Shot™ MAX Efficiency™ DH5α-T1 <sup>R</sup> Competent Cells	Invitrogen™	12297016
3rd generation virus	This paper	N/A
<b>Chemicals, peptides, and recombinant proteins</b>		
DYn-2	Cayman Chemical	Cat# CAY11220
Influenza Hemagglutinin (HA) Peptide	Sigma-Aldrich	Cat# I2149
Puromycin, Dihydrochloride, Cell Culture-Tested	Sigma-Aldrich	Cat# 540411
Hygromycin B	MP Biomedicals	Cat# 19417080

(Continued on next page)



**Continued**

REAGENT or RESOURCE	SOURCE	IDENTIFIER
N-Ethylmaleimide	Sigma-Aldrich	Cat# E3876
Thymidine	Sigma-Aldrich	Cat# T9250
RO-3306	Sigma-Aldrich	Cat# SML0569
Nocodazole	Sigma-Aldrich	Cat# M1404
MG-132	AdipoGen	Cat# AG-CP3-0011
Recombinant human EGF	Gibco	Cat# PHG0311
N-2 supplement (100x)	Gibco	Cat# 17502048
FGF	ReproTech	Cat# AF-100-18B
B-27 <sup>TM</sup> Supplement (50x), minus Vitamin A	Gibco	Cat# 12587010
Dulbecco's Modified Eagle's Medium - low glucose	Sigma-Aldrich	Cat# D5921
Dulbecco's Modified Eagle's Medium - high glucose	Sigma-Aldrich	Cat# D6429
Penicillin-Streptomycin (10.000 U/mL)	Gibco	Cat# 15140122
Vitronectin XF <sup>TM</sup> Kit with ReLeSR <sup>TM</sup>	STEMCELL technologies	Cat# 07191
mTeSR Plus	STEMCELL technologies	Cat# 05825
CloneR <sup>TM</sup>	STEMCELL technologies	Cat# 05888
Pierce <sup>TM</sup> ECL Western Blotting-Substrat	Thermo Scientific <sup>TM</sup>	Cat# 10455145
Pierce <sup>TM</sup> ECL Plus Western Blotting-Substrat	Thermo Scientific <sup>TM</sup>	Cat# 11517271
cOmplete <sup>TM</sup> , Mini, EDTA-free Protease Inhibitor Cocktail	Roche	Cat# 11836170001
PhosSTOP <sup>TM</sup>	Roche	Cat# 4906845001
Benzonase	Millipore	Cat# 70746-3
MEM	Thermo Scientific <sup>TM</sup>	Cat# 31095-029
DiD	Biotium	Cat# 60014
HEPES	Sigma Aldrich	Cat# H0887-20ML
D-glucose	Sigma Aldrich	Cat# G8644-100ML
Pierce <sup>TM</sup> 16% Formaldehyde (w/v), Methanol-free	Thermo Scientific <sup>TM</sup>	Cat# 28908
$\alpha$ -Thioglycerol	Sigma Aldrich	Cat# M1753
MOPS running buffer	Life Technologies	Cat# NP0001
NuPage Gels 10well, 1,5mm	Life Technologies	Cat# NP0335
NuPAGE 4-12% 1,5mmx15well	Life Technologies	Cat# NP0336
IGEPAL	Sigma Aldrich	Cat# I8896
D-Luciferin, Potassium Salt	BioVision	Cat# 7903-1G-BV
mTeSR <sup>TM</sup> Plus	STEMCELL Technologies	Cat# 100-0276
BSA	Roth	Cat# T844.2
HANKS' BALANCED SALT SOLUTION, HBSS+	Sigma Aldrich	Cat# 55037C-1000ML
O.C.T. Compound, Kryoeinbettmedium	DKFZ stock material	Cat# 14291
L-Glutamic acid- <sup>15</sup> N	Sigma Aldrich	Cat# 332143
Pyridoxal 5'-phosphate monohydrate	Sigma Aldrich	Cat# 82870
Propidium Iodide Solution	Sigma Aldrich	Cat# P4864
SiR-Actin	Cytoskeleton Inc.	Cat# SC001
SiR-tubulin	Cytoskeleton Inc.	Cat# SC002
SPY555-DNA	Cytoskeleton Inc.	Cat# SC201
NucBlue Live cell Stain ReadyProbes	Invitrogen <sup>TM</sup>	Cat# R37605
FxCycle <sup>TM</sup> Violet Ready Flow <sup>TM</sup> Reagent	Invitrogen <sup>TM</sup>	Cat# R37166

(Continued on next page)

**Continued**

REAGENT or RESOURCE	SOURCE	IDENTIFIER
Vectashield® Hard + Set Mounting Medium (Anti Fading) w/DAPI	Linaris	Cat# H-1500
ProLong Glass Antifade Mountant with NucBlue Stain	Invitrogen™	Cat# P36983
Pierce™ Anti-HA Magnetic Beads	Thermo Scientific™	Cat# 88836
Dynabeads™ Protein G for Immunoprecipitation	Invitrogen™	Cat# 10003D
μ-slide 8 chamber	Ibidi GmbH	Cat# 80826
12 Well Chamber, removable	Ibidi GmbH	Cat# 81201
Opti-MEM™	Gibco™	Cat# 31985062
geneticin (G418 sulfate)	Thermo Scientific™	Cat# 10131035

**Critical commercial assays**

Click-iT™ Plus Alexa Fluor™ 647 Picolyl Azide Toolkit	Invitrogen™	Cat# C10643
Alexa Fluor™ 488 Azide	Invitrogen™	Cat# A10266
Click-iT™ Cell Reaction Buffer Kit	Invitrogen™	Cat# C10269
DCFDA/H2DCFDA - Cellular ROS Assay Kit	Abcam	Cat# ab113851
QuickChange II XL site-directed mutagenesis kit	Aligent	Cat# 200521
Quik Change Lightning	Aligent	Cat# 210518

**Experimental models: Cell lines**

LN-229	ATCC®	ATCC® CRL-2611™
U-87 MG	ATCC®	ATCC® HTB-14™
U-251 MG	ATCC®	ATCC® HTB-17™
MDA-MB-231	ATCC®	ATCC® HTB-26™
HEK293FT	Dr. Rainer Will (Stable Isogenic Cell Line Service, DKFZ)	N/A
mGB2	<a href="#">Costa et al., 2021</a>	N/A
StemRNA™ Human iPSC 771-3G	Stemgent™	RCRP005N

**Experimental models: Organisms/strains**

C57BL/6N	Janvier Labs	N/A
----------	--------------	-----

**Oligonucleotides**

sgRNA human BCAT1 exon3: CACGGA TCATATGCTGACGG	This paper	N/A
sgRNA control: GCGAGGTATTCGG CTCCGCG	This paper	N/A
BCAT1-SXXS-fwd: GGTACAGCCTCTG TT GTTAGCCAGTTTCT	This paper	N/A
BCAT1-SXXS-rev: AGAACTGGGCTAAC AACAGAGGCTGTACC	This paper	N/A
BCAT1-K222A-fwd: GGTGGAAGTGGGGA CTGCGCGATGGGAGGGAATTACG	This paper	N/A
BCAT1-K222A-rev: CGTAATTCCTCCCA TCGCGCAGTCCCCAGTTCCAC	This paper	N/A
BCAT1-CRISPR-resistant-fwd: CACGGAT CATATGCTGACCGTCGAGTGGTCCTCA GAGTTTGG	This paper	N/A
BCAT1-CRISPR-resistant-rev: CCAAACCTGAGGACCACTCGACGGTCAGCATAT GATCCGTG	This paper	N/A
sgRNA mouse Bcat1: GCTGACCACATG CTGACGTGG	This paper	N/A

(Continued on next page)

**Continued**

REAGENT or RESOURCE	SOURCE	IDENTIFIER
<b>Recombinant DNA</b>		
LentiCRISPRv2	Addgene	Cat# 52961
psPAX2	Addgene	Cat# 12260
pMD2.G	Addgene	Cat# 12259
TLCV2	Addgene	Cat# 87360
pLVX-EF1a-Neuromodulin-IRES-Puromycin	Addgene	Cat# 134666
pLVX-puro	Clontech	Cat# 632164
pSpCas9(BB)-2A-GFP (PX458)	Addgene	Cat# 48138
pCCL-CellCycle	Addgene	Cat# 132429
pLenti PGK V5-LUC Neo	Addgene	Cat# 21471
<b>Software and algorithms</b>		
FlowJo V10	FlowJo, LLC, USA	<a href="https://www.flowjo.com/">https://www.flowjo.com/</a>
GraphPad Prism version 9.0.0	GraphPad Software	<a href="http://www.graphpad.com">http://www.graphpad.com</a>
Fiji/ImageJ	ImageJ Software	<a href="https://imagej.net/Fiji">https://imagej.net/Fiji</a>
RStudio	RStudio	<a href="https://www.rstudio.com/">https://www.rstudio.com/</a>
Affinity designer	Serif Europe	<a href="https://affinity.serif.com/en-gb/">https://affinity.serif.com/en-gb/</a>

**RESOURCE AVAILABILITY**

**Lead contact**

Further information and requests for resources and reagents should be directed to the lead contact, Dr. Bernhard Radlwimmer ([b.radlwimmer@dkfz-heidelberg.de](mailto:b.radlwimmer@dkfz-heidelberg.de)).

**Materials availability**

All plasmids and cell lines generated in this study are available from the [lead contact](#) with a completed Materials Transfer Agreement.

**Data and code availability**

- Mass spectrometry data reported in this paper will be shared by the [lead contact](#) upon request.
- This paper does not report original code.
- Any additional information required to reanalyze the data reported in this paper is available from the [lead contact](#) upon request.

**EXPERIMENTAL MODEL AND SUBJECT DETAILS**

**Cell lines and culture conditions**

U-251 MG (U251), LN-229 MG (LN229), U-87 MG (U87) and MDA-MB-231 were obtained from ATCC. 293FT were obtained from the clone repository facility (DKFZ, Dr. Rainer Will). U251, LN229, U87 and MDA-MB-231 were cultured in DMEM with 1000 mg/mL glucose, 0.5 mM L-glutamine, 1x penicillin-streptomycin (P/S) and 10% fetal calf serum (FCS). 293FT cells were grown as adherent cells in DMEM high glucose, supplemented with 10% FCS, 1X MEM non-essential amino acids, 1X Glutamax and 1 mM sodium pyruvate. Cell lines were maintained in an incubator at 37°C and 10% CO<sub>2</sub> for U251MG, LN229, U87 and MDA-MB-231 and 5% CO<sub>2</sub> for 293FT. StemRNA Human iPSC 771-3G from Reprocell (kind gift from Dr. Lena Kutscher DKFZ, Heidelberg, Germany) were cultured under standard conditions in 6 well plates coated with Vitronectin XF and mTeSR plus from STEMCELL. The media was refreshed every 48h until colonies were ready to be passaged. Passaging was performed using ReLeSR (STEMCELL) followed by gentle dissociation into smaller colonies and replating 1:50. iPSC were not used after 15 passages and were frequently checked for normal Karyotype using the HumanCytoSNP-12 v2.1 BeadChip (Illumina).

**Mouse glioblastoma model**

For the syngeneic mouse experiments, C57BL/6 female 8–10-week-old mice from Janvier labs were used. The previously described GFP-positive, Luciferase-expressing mGB2 cells ([Costa et al., 2021](#)) were dissociated into a single cell suspension and resuspended to a final concentration of  $1.5 \times 10^5$  cells per  $\mu$ L PBS.  $2\mu$ L of the cell suspension were injected stereotactically into the mouse brain while under isoflurane induced anesthesia, 2mm lateral of the bregma and 3mm d. The injection was performed with a flow rate of 0.2 $\mu$ L/min using a 10- $\mu$ L microsyringe (World Precision Instruments, Inc, Sarasota, FL, USA). *In vivo* bioluminescent imaging was performed using the IVIS system weekly from the 4th week post-injection. The mice were anesthetized using isoflurane and injected

with 150mg/kg of luciferin in PBS interperitoneally. The measurement was performed 10min after the injection with a 1min exposure. All animal experiments were carried out according to governmental and institutional guidelines and authorized by the local authorities (Regierungspräsidium Karlsruhe, Germany, permit number: G314-19).

### GLICO model and organoid culturing

Human cerebral organoids were produced according to the previously described protocol (Lancaster and Knoblich, 2014) with slight modifications. Briefly, hiPSC cells were seeded into ULA U-bottom 96 well plates to produce embryoid bodies (EBs). The EBs were cultured in low FGFb medium (4ng/mL) for 3 days after which FGFb-free medium was used for an additional 2 days. Neural induction was performed for 6 days or until clear signs of neural induction were observed. Organoids were embedded in 20–30  $\mu$ L of matrigel and cultured in RA-free medium for 7 days, after which RA was added to the medium and further culturing was performed on an orbital shaker. For further experiments, organoids were used after day 20 of culturing.

The GLICO model (Lancaster and Knoblich, 2014) was established using LN229 spheroid cultures. For this, the GFP-expressing LN229 cells were placed in ULA T75 flasks in stem-cell enrichment medium (DMEM/F12, 15mM HEPES, 1% Glutamax, 1% Penstrep, 1% N2 supplement, 2% B27 supplement, 20ng/mL recombinant EGF and 20ng/mL recombinant FGFb). Cells were passaged under these conditions for a minimum of 2 weeks prior to use. For the establishment of the GLICO model, individual mature cerebral organoids were co-cultured with 100.000 GFP-positive LN229 cells for 24h. Following the incubation, non-attached cells were washed and the organoids were further cultured individually for 14 days until tumor cell growth was evident under the fluorescent microscope.

### METHOD DETAILS

#### Generation of BCAT1 constructs

BCAT1 cDNA obtained previously by Tönjes et al. (2013). BCAT1 was N-terminally tagged with an HA-tag by amplifying BCAT1 using primers containing the HA-tag sequence at the N-terminus (see oligonucleotide list). For lentivirus transduction, HA-BCAT1 or BCAT1 were inserted into the lentivirus delivery vector pLVX-puro using XhoI and XbaI or to the pLVX-IRES-hygro vector using BstXI and BamHI restriction sites.

BCAT1 mutants SXXX (C335S/C338S) and K222A, as well as constructs resistant to Cas9 were created by site-directed mutagenesis using the QuikChange Lighting (# 210518, Aligent) or QuickChange II XL (#200521, Agilent) site-directed mutagenesis kits following the manufacturer protocol and the primers listed in the primer table. DNA sequences were verified by GATC (Eurofins Genomics) sequencing services using cycle sequencing on ABI 3730XL machines.

#### Lentiviral production

A 2<sup>nd</sup> generation lentiviral packaging system was used for lentiviral production with the packaging vector psPAX.2 (Addgene, #12260) and envelope vector pMD2.G (addgene, #12259). One day prior to transfection,  $5 \times 10^6$  293T cells were seeded in 10 cm dishes. Medium was refreshed 2 h before transfection with 5 mL medium. Cells were transfected with 8  $\mu$ g DNA, composed of 4  $\mu$ g sgRNA vector, 2  $\mu$ g packaging and 2  $\mu$ g envelope vector. The DNA was mixed 3:1 with Polyethylenimine (PEI) in OptiMEM medium in a final volume of 250  $\mu$ L. After an incubation of 15 min at room temperature the transfection mix was added to the cell dishes dropwise. 24 h after transfection, the medium was refreshed. Viral supernatant was collected 72 h post transfection and filtered using a 0.45  $\mu$ m syringe filter. The solution was centrifuged at 1800  $\times$  g for 90 min at 4°C. The pelleted virus was resuspended in 100  $\mu$ L OptiMEM and stored at –80°C.

#### Generation of CRISPR/Cas9 knockout cell lines

Guide RNAs (sgRNAs) targeting exon 3 of BCAT1, were designed using online tools (<http://crispr.mit.edu/>). Oligos coding for the sgRNAs targeting BCAT1 (CACGGATCATATGCTGACGG) or a non-targeting control sgRNA (Control) were cloned into the lentiCRISPRv2 vector as described in (Sanjana et al., 2014). The lentiCRISPRv2-sgRNA were delivered to U251, LN229 and MDA-MB-231 cells by lentiviral transduction followed by puromycin selection for two days. Then, single clones were generated by serial dilution into 96-well plates. Single clones were grown and expanded in media containing puromycin for at least 10 days. Clones were screened by WB for efficient total BCAT1 depletion. Homozygous knockout was confirmed in selected clones by PCR and sequencing of genomic DNA.

To knockout BCAT1 in hiPSC, we cloned the sgRNA targeting BCAT1 into the pSpCas9(BB)-2A-GFP (PX458) as described in (Ran et al., 2013). iPSCs were electroporated with 5 $\mu$ g of plasmid DNA using the Neon Nucleofection System according to standard protocols. Immediately after electroporation, 500 cells were placed in 10cm dishes containing mTeSR plus supplemented with CloneR (STEMCELL). Media was refreshed every 2 days until single colonies could be detected. Single colonies were then expanded, and screened for homozygous BCAT1 deletion, as described above.

#### Immunofluorescence

For immunolocalization of BCAT1, cells were seeded in coverslips or in  $\mu$ -slides (12 chamber removable, ibidi) and grown for 24–48 h. Cells were washed with PBS and fixed with 4% paraformaldehyde (PFA) for 15 min at room temperature (RT). After washing with PBS, cells were permeabilized with 0.2% Triton X-100, 1% BSA in PBS for 20 min and blocked for 30–60 min in blocking buffer (3% BSA 0.1% Triton X-100 PBS) at RT. The primary antibody was diluted in blocking buffer and incubated overnight at 4°C in a humidified



chamber. After washing 3 times with PBS, the secondary antibody (1:1000 in PBS) was incubated for 1–2 h at RT protected from the light. To counterstain for F-actin, samples were washed once and stained with Acti-stain™ 670 phalloidin (Cytoskeleton, Inc) for 30 min at RT. Afterwards, cells were washed two times with PBS, dipped in water and mounted using Vectrashield with DAPI.

For characterization of mitotic spindles by immunofluorescence, LN229 cells were grown on glass coverslips and fixed with 4% formaldehyde in PBS for 10 min at room temperature (RT). After fixation, coverslips were washed with PBS, followed by permeabilization with 0.15% Triton X-100 in PBS for 10 min. Permeabilized cells were blocked in 5% FCS in PBS for 60 min. Primary antibody incubations were performed in 1% BSA in PBS at 4°C overnight. After washing with PBS, cells were incubated with secondary antibodies as well as Phalloidin 647 in 1% BSA in PBS for 60 min at RT. Coverslips were mounted with mounting medium with DAPI (DAKO). Imaging was performed using a LSM800 (Zeiss) confocal laser-scanning microscope equipped with a 63x, 1.4 NA oil objective. Full z-stacks of fixed LN229 cells in metaphase were acquired using the Airyscan detector and 500 nm z-distance between planes, followed by Airyscan Processing with the Zen blue software. For the 3D reconstructions of dividing cells, the distance between both centrosomes was measured. Exactly in the middle between both centrosomes the cell was divided in 2 hemispheres by an orthogonal plane. The volume of the DNA staining and of the microtubule staining was measured in both hemispheres. The larger value was divided by the lower value. A value of 1 indicates perfect symmetry of both hemispheres. Values > 1 indicate increasing asymmetry. Images were analyzed and processed by Imaris and Metamorph software.

Immunofluorescence of GFP-BCAT1 was performed by transient transfection of GFP-BCAT1 in LN229 cells, growing on coverslips. After fixation, staining protocol for tubulin was followed as described above. Airyscan z-stacks of metaphase and anaphase cells were acquired using 140 nm z-distance.

### Live cell imaging

For live-cell imaging of LN229 and iPSC, cells were seeded in glass bottom  $\mu$ -slides (ibidi). Prior to imaging, fresh media was added with NucBlue (Invitrogen, 1 drop per 2.5 mL of media) or SPY555-DNA (1:10 000). Cells were imaged in a Leica SP8 confocal microscope equipped with incubation chamber (37°C 5% CO<sub>2</sub>) using a 40x/1.30 HC PL APO CS2 (oil) objective or using an inverted Axio Observer.Z1 with Yokogawa CSU-X1 Spinning Disk.

Live cell images of cleavage furrow were generated using a LSM800 (Zeiss) confocal laser-scanning microscope equipped with a 63x, 1.4 NA oil objective, Airyscan detector (Zeiss) and Zen blue software (Zeiss). Cells were seeded in 8 well  $\mu$ -slide ibidi chambers (ibidi) and incubated with 50 nM of SiR-actin 18h overnight before image acquisition. On the next day NucBlue (Hoechst33342) was added 20min prior to the experiment. Cells undergoing spontaneous mitosis in anaphase were imaged as z-stacks (including 5 planes with 1  $\mu$ m z-distance) every 15 s until cleavage furrow was fully closed and cells started to undergo cytokinesis. For analysis of cleavage furrow closure the diameter of the contractile ring in the actin channel was measured. The measurement was stopped when the gap was fully closed, or no further closure was possible due to obstruction by a chromosome.

For Airyscan live cell imaging of GFP-BCAT1 localization to the mitotic spindle the same microscopy setup was used, as described above. LN229 cells were seeded in an 8 well  $\mu$ -slide ibidi chamber and co-transfected the next day with low DNA amounts of GFP-BCAT1 and EB3-tomato. 24h after transfection full z-stacks of a dividing cell were acquired every 8 min, using 500 nm z-distance. Time-lapse Images were analyzed and processed by Imaris and Metamorph software.

For live-cell imaging of mitotic cells in GLICO model, tumor-bearing organoids were stained with low concentrations of SiR-tubulin (1:5000) and SPY555-DNA (1:5000) for 16hr. then, to prevent displacement of the sample during microscopy, organoids were placed over a drop of matrigel on a 35mm  $\mu$ -dish (ibidi) and filled up with fresh media without dyes. GLICOs were imaged in a Leica SP8 confocal microscope equipped with incubation chamber (37°C 5% CO<sub>2</sub>).

### Click-iT™ EdU cell proliferation assay

Cells were seeded in 6-well plates and treated with 10  $\mu$ M EdU for 4–8 h. Cells were washed with PBS, detached with trypsin and fixed with 4% PFA for 15 min. Fixed cells were washed with 1% BSA PBS and permeabilized for 30 min using 0.1% (v/v) Triton X-100 PBS. Click-iT detection was performed as indicated by the manufacturer (Invitrogen) using either Alexa 488 azide or Alexa 647 pycocyl-azide. The latter was applied when Click-iT was used in combination with propidium iodide (PI) for cell cycle analysis. Cytometric analysis was performed with a FACS Canto II (BD biosciences). Acquisition was stopped after 10,000 single cells were measured. Data was analyzed using Flowjo software (Flowjo LLC, V10).

### Tissue preparation

Upon reaching the end criteria according to the animal permit or at the end of the experiment in cases of no detectable tumor growth, the mice were euthanized using CO<sub>2</sub> and the brain was fixed in 4% PFA overnight. Following the fixation, brains were dehydrated in 30% sucrose for 48h and cryopreserved in OCT until sectioning.

For immunofluorescence of mouse brain tissues, 15  $\mu$ m cryopreserved tissue sections were obtained using a cryotome at –30°C. The sections were dried at room temperature and excess OCT was removed by incubating the slides in 37°C PBS for 10min. Slides were permeabilized and blocked for 1h at room temperature in blocking buffer (PBS, 5% BSA, 0.5% Triton X-, 0.02% NaN<sub>3</sub>). Primary antibody staining was performed in 5 times diluted blocking buffer at 4°C. After 3 washes with PBS 0.1% Tween 20, secondary antibodies were applied at a 1:1000 dilution for 1h at room temperature. The slides were washed an additional 3 times and mounted using Vectrashield with DAPI. Images were obtained using the Leica SP8 confocal microscope.

### Synchronization of cells in mitosis

Cells were synchronized at G1/S using double thymidine block (2TB). Cells were seeded in 15cm dishes. When the cells reached 60% confluency, 2.5mM of thymidine was added and incubated for 16 h. To release from thymidine block, cells were washed twice with serum-free media and incubated for 9–10h with complete media before treating again with 50 ng/mL of Nocodazole or 6  $\mu$ M RO-3306 for 16h. For co-immunoprecipitation experiments, U251 cells expressing HA-BCAT1 or HA-EV were treated with Nocodazole and collected by the shake-off method. Collected mitotic cells were placed on ice, spun for 5 min at 1000 rpm at 4°C and incubated with 100 mM NEM PBS for 5min. After another centrifugation, pellets were resuspended in lysis buffer (1% Triton X-100, TBS) containing 10 mM NEM and protease inhibitors cocktail.

For phosphoproteomics experiments, cells were synchronized using one thymidine block and RO-3306 as described above. Then, cells were released from RO-3306 by washing 2 times with serum free media and allowing them to enter mitosis for 30–45 min before mitotic shake-off.

### KNL1-pMELT, AURKB localization and chromosome alignment assays

Chromosome alignment assays were performed as described in (Smith et al., 2019). Briefly, cells growing in 10 mm coverslips were released from thymidine block for 7 h and synchronized at the G2/M boundary with RO-3306 (9 $\mu$ M) for 2h. Then, cells were washed three times and incubated for 15 min in complete media, after which MG-132 (10  $\mu$ M) was added for additional 30 min to prevent mitotic exit. Cells were washed for 1 min with pre-extraction buffer (0.1% Triton X-100, 100 mM Pipes pH 6.8, 1 mM MgCl<sub>2</sub> and 5mM EGTA) and then fixed with 4% PFA for 10 min. PFA was then quenched for 5 min with glycine pH 8.6 and then staining with the indicated antibodies was performed as described above.

For KNL1-pMELT (kind gift from Geert Kops, Hubrecht Institute-KNAW, NL) analysis, whole coverslips were imaged using a Zeiss AxioScan 7 with 40x objective and 5 z stack were acquired. After background subtraction (rolling ball radius = 50 pixels), mitotic cells were segmented based on tubulin signal or identified manually, and the mean fluorescence intensity (MFI) of the KNL1-pMELT channel was extracted. The experiment was repeated in at least 3 independent coverslips for each condition.

For chromosome alignment experiments and AURKB localization experiments, imaging was performed on a Leica SP8 laser-scanning microscope, using a 63x objective, 12-bit pixel depth, and 500nm Z-distance. Scoring was based on the counted misaligned chromosomes: aligned (0 misaligned chromosomes), mild (1–2 misaligned chromosomes), moderate (3–5 misaligned chromosomes) or severe (>6 misaligned chromosomes). Quantification of AURKB signal intensity at centromeres was done using ImageJ. After background subtraction (rolling ball radius = 50 pixels), the centromeric region was segmented from anti-CREST channel using “Otsu” thresholding and the MFI at the segmented area was extracted from CREST and AURKB channels. The ratio of AURKB to CREST was calculated for each individual cell by dividing AURKB MFI by CREST MFI. The experiment was performed in 3–4 independent coverslips.

### Co-immunoprecipitation and MS

500–1000  $\mu$ g of protein was pre-cleared with 20  $\mu$ L of Dynabead protein G for 1 h at 4°C with gentle rotation. The beads were removed and lysates were incubated with 50 $\mu$ L Dynabeads and 2–10  $\mu$ g of the indicated antibody, or isogenic IgG control, and let rotating at 4°C overnight. After washing 4 times with 0.1% Triton X-100 TBS, samples were eluted directly in sample buffer or with 50 mM glycine pH 2.8 for 10 min at RT with shaking at 1200 rpm. Immunoprecipitation of HA-BCAT1 was performed with anti-HA magnetic beads (Pierce) for 3–4 h at 4°C with gentle rotation. The beads were then washed 4 times with 0.1% Triton X-100 TBS and samples were eluted with 200  $\mu$ g/mL of HA-peptide in PBS for 30 min at 25°C with shaking at 1200 rpm. Co-IP proteins were analyzed by Western blot and immunoblot with the indicated antibodies or sent for MS analysis.

Data analysis was carried out by MaxQuant (version 1.6.14.0). Peptides and proteins were identified by MSMS based on an FDR cutoff of 0.01 on peptide level and 0.01 on protein level. Match between runs option was enabled to transfer peptide identifications across Raw files based on accurate retention time and m/z. Quantification was done using a label free quantification approach based on the MaxLFQ algorithm (see Cox et al., 2014).

For the GSEA enrichment plots of G2-to-M Checkpoint and Mitotic Spindle signatures, HA-BCAT1 bound proteins were ranked using the average log<sub>2</sub> LFQ value (N = 3) together with the unbound proteins identified in the input (assigned negative log<sub>2</sub> LFQ values). The ranked list was used to perform a pre-ranked GSEA analysis with the MSigDB Hallmark gene sets. The G2-to-M Checkpoint and Mitotic Spindle gene sets were found to be in the top 10 enriched signatures, with NES of 2.3 and adjusted p values smaller than 0.01. For display of the network of HA-BCAT1 bound proteins, Mitotic spindle and Kinetochore proteins were extracted from Gene Ontology Cellular Compartment terms. Proteins that were found in HA-BCAT1 co-IP are shown in red and those found in the input but not bound to HA-BCAT1 were shown in blue.

### Phosphoproteomics

For the phosphoproteomic and proteomic analysis, ~ 400  $\mu$ g protein per sample was collected and submitted for MS analysis. Samples were digested with Lyc-C and trypsin in 8M Urea and desalted using Sep-Pak cartridges. Phosphopeptide enrichment was performed using immobilized metal affinity chromatography (Fe-IMAC) and the peptides analyzed by LC-MS/MS.

Data was initially analyzed by MaxQuant (as describe above). Further data analysis was performed using the LFQ values with exclusion of potential contaminants. Differential phospho-site representation was determined in R using the phosR package (Kim et al.,

2021) after filtering for phosphosites that could be identified in at least 50% of the technical replicates within at least 1 of the conditions. Data was normalized using variance stabilizing normalization (vsr) and imputation of missing values was performed as a combination of site- and condition-specific imputation and paired end imputation by minimal probability distribution, as described previously (Kim et al., 2021). The KSEA analysis (Kinase-Substrate Enrichment Analysis) was performed using the publicly available KSEA software (Wiredja et al., 2017) by utilizing PhosphoSitePlus and NetworkKIN databases with a set substrate count minimum of 5 using the differential phospho-site representation values.

The PTMSigDB analysis was performed using the publicly available ssGSEA (single sample Geneset enrichment analysis) R package (Krug et al., 2019). GCT files were produced using log transformed normalized and imputed data and then analyzed using the human uiprot GMT collection (v1.9.1) to produce enrichment score GCT files for the most prominent signatures.

### DYn-2 labeling for detection of sulfenic acids

Labeling of sulfenic acids in mitotic cells was adapted from (Truong et al., 2016). For detection of sulfonylation in the cell cycle by flow cytometry, LN229 were seeded in 10 cm dishes. After washing 2 times with media without serum, cells were labeled with 4mM DYn-2 in media without serum for 30 min at 37°C 5% CO<sub>2</sub> with constant shaking. Cells were then washed with PBS, fixed with ice-cold 70% ethanol and stored at –20°C. Residual ethanol was washed with PBS and then click chemistry was performed using the Click-iT reaction kit (Invitrogen) with Alexa 488-azide for 30 min at RT. After another wash, mitotic cells were stained with pS10-Histone3-Alexa647 (pH3-647, biolegend) diluted 1:100 in 3% BSA PBS for 60–90min at RT. Cells were then washed twice and DNA was stained using FxCycle violet (Molecular probes) for 30 min before flow cytometry analysis. For analysis of mitotic cells, cells were first synchronized using a nocodazole block (as described above) and harvested using the mitotic shake-off method. Acquisition was performed in a BD LSR Fortessa and analyzed with Flowjo. For detection of PP1 sulfonylation, LN229 cells were harvested by mitotic shake-off and labeled with 5mM DYn-2 (or DMSO) for 1hr 37°C 5% CO<sub>2</sub>. After washing 3 times with ice-cold PBS, cells were lysed in lysis buffer (50 mM HEPES, 150 mM NaCl, 1% (vol/vol) Igepal and 8 mM DTT, pH 7.5) for 30 min on ice. Lysates were subjected to immunoprecipitation as describe above. Click-iT chemistry was performed on beads using the Click-iT reaction kit (Invitrogen) with Biotin-azide for 1hr at 25°C. Click-iT reaction was quenched with the addition of 1mM EDTA and samples were eluted from beads with 2xLDS by boiling at 95°C for 10min. Sulfonylation was detected using Streptavidin-HRP (GE, healthcare 1:10,000 in TBS-T) and the same membrane was then incubated with anti-PP1 followed by fluorescence detection using anti-mouse 647. Sulfonylated PP1 was normalized to total immunoprecipitated PP1 of each sample.

### HA-BCAT1 overexpression and purification for *in vitro* transaminase assays

293FT cells were transduced by lentivirus with the pLVX-puro-HA-BCAT1 variants or empty vector and selected with puromycin for 48 h. Cells stably expressing HA-BCAT1<sup>wt</sup>, HA-BCAT1<sup>SXXXS</sup> or HA-BCAT1<sup>K222A</sup> were adapted to grown in suspension by gradually decreasing the content of FCS in the media (10%, 5%, 2%) until complete removal. Suspension cells were then transferred into spinner flasks (Wheaton). After reaching a density of 1 × 10<sup>6</sup>/ml, cells were pelleted by centrifugation at 900 rpm at 4°C, washed once with ice-cold PBS and frozen at –80°C. Cell pellets were lysed in Pierce IP buffer (with proteinase inhibitors cocktail, Roche) for 30 min at 4°C with gentle rotation and cleared by centrifugation at 13,000 rpm for 20 min at 4°C. Cleared proteins were incubated with anti-HA magnetic beads for 3 h at 4°C with gentle rotation. Beads were then washed 3 times with 0.05% Tween 20 TBS (TBS-T) and 1 time with de-ionized water. The HA-BCAT1 variants were eluted with HA-peptide (200 µg/mL in PBS) for 30 min at 30°C while shaking at 600 rpms. Eluted HA-BCAT1 was further concentrated using the Pierce concentration columns MWKO 10K. HA-BCAT1 purity was determined by SDS-PAGE and Coomassie staining. Concentration was estimated photometrically using a Nanodrop instrument.

### *In vitro* BCAT1 transaminase assay

The BCAT1 activity assay was modified from previously reported (McBrayer et al., 2018). Briefly, <sup>15</sup>N-labeled glutamate was generated from a transfer of the amino group of the <sup>15</sup>N-labeled BCAAs to α-ketoglutarate (α-KG) which is catalyzed by the recombinant HA-BCAT1. Assays were performed for 11 min at 37°C in 200 µL system of 100 mM Tris buffer, pH 7.4, containing 50 µM pyridoxal 5'-phosphate, 5 mM DTT, 5 mM <sup>15</sup>N-labeled isoleucine, 600 ng recombinant HA-BCAT1, 500 µM α-KG (all chemicals are purchased from Sigma-Aldrich, Darmstadt, Germany). After the assay, the solutions were immediately stored at –80°C until further analysis. For quantitative analysis of metabolites by gas chromatography-mass spectrometry (GC-MS), 20 µL reaction solution was added with 180 µL –20°C methanol:H<sub>2</sub>O (8:1) with 2 µg/mL D<sub>6</sub>-pentanedioic acid (as internal standard), followed by vortex for 10 min, at 1400 rpm, 4°C and centrifugation for 10 min, at 17,000 g, 4°C. Afterward, 80µL supernatant was transferred to a GC-compatible vial and then dried at 4°C under vacuum in a CentriVap Concentration System (Labconco, Kansas City, Missouri). GC-MS measurements were performed as described (Battello et al., 2016). Briefly, the metabolites were derivatized firstly by methoxyamine hydrochloride, then by N-tert-Butyldimethylsilyl-N-methyltrifluoroacetamide (MTBSTFA). Metabolite separation was performed using an Agilent 7890B gas chromatograph equipped with a 30 m DB-35ms + 5 m Duraguard capillary column (Agilent), followed by measurement on Agilent 5977B MSD system. Processing of GC-MS chromatograms and calculation of mass isotopomer distributions was performed using the Metabolite Detector software (Hiller et al., 2009). Total glutamate and <sup>15</sup>N-labeled M1 glutamate were quantified to signify BCAT1 transaminase activity.

### Determination of glutathione

LN229 cells were seeded in triplicate in 6 well plates and synchronized using one thymidine block and nocodazole as describe above. After washing with 0.9% NaCl solution, 100 $\mu$ L of ice-cold extraction fluid [ $^{13}\text{C}_2$   $^{15}\text{N}_1$ -labeled GSH (5  $\mu$ g/mL), N-Ethylmaleimide (85 mM) and  $\text{Na}_2\text{EDTA}\cdot 2\text{H}_2\text{O}$  (0.5 mg/mL) in  $\text{H}_2\text{O}$ ] was added, followed by 100 $\mu$ L of ice-cold 5% trichloroacetic acid. Cells were scraped into eppies and vortexed (4°C, 14000rpm) for 10 min. After centrifugation (4°C, 17000g) for 5 min, samples were transferred to plastic LC vials and subjected to LC/MS analysis.

### LC-MS analysis

Glutathione measurement was performed using Bruker impact QTOF mass analyzer (Bruker Corporation, Massachusetts) coupled with Agilent 1260 Infinity II LC System (Agilent Technologies, California). 10  $\mu$ L of metabolite extract was injected using HPLC autosampler. The chromatographic separation was achieved using ATLANTIS T3 column (Waters, Milford, MA) that was eluted at 300  $\mu$ L/min with a 40 min linear gradient of mobile phase A (water with 10 mM ammonium formate and 0.1% formic acid) and mobile phase B (acetonitrile with 0.1% formic acid). High resolution full scan MS data (50–1300 m/z) in positive ion mode was acquired using Compass HyStar software package (Bruker Corporation, Massachusetts). MS conditions were set as follows, source temperature: 250°C, Capillary voltage: 3500 V, Nebulizer: 0.4 Bar, dry gas: 4 L/min, endplate offset: 500V, rolling average: 3, and spectra rate: 1Hz. Compass Data Analysis software was used for manual inspection of chromatograms and integration of peak areas.

### SDS-PAGE and western blot

Proteins were prepared in NuPAGE LDS Sample Buffer (4X) with NuPAGE reducing agent (10x) and were heated at 70°C for 10 min before loading onto the gel. For non-reducing gels, the reducing agent was omitted. Proteins were separated by 4–12% Bis-Tris SDS-PAGE at 200mV –170 mA and transferred PVDF membranes. Membranes were blocked 1h in 5% milk TBS-T and incubated overnight at 4°C with the primary antibody diluted in 1% milk TBS-T. After washing 3 times with TBS-T, membranes were incubated 1h with HRP conjugated secondary antibody in 1% milk TBS-T. After another 3 washes, 1:1 mix of the ECL mixture was added and chemiluminescence was detected using an ECL chemiluminescence imager (Chemostar V60+, INTAS).

### Transwell cell migration assay

Migration capacity of U251 Control and BCAT1-KO cells was assessed using Costar Polycarbonate Membrane Transwell inserts (8  $\mu$ m pores, Cat #3422, Corning). Cells were seeded in 6-well plates and starved in serum-free media overnight. Then, 10,000 cells were transferred into pre-wet insert cups and allowed to migrate for 24 h. Media containing 10% FCS was used as chemoattractant. Cells that migrated into the membrane were fixed in methanol, followed by hematoxylin staining and sequential dehydration in 80% and 100% ethanol. Per insert, 5 fields of view were imaged using a 20x objective in a Zeiss Axio Vert.A1. Migrated cells were counted by eye.

### In situ brain slice invasion assay

The *in-situ* brain invasion assay was performed as described in [Eisemann et al. \(2018\)](#). Briefly, 1 million LN229 control and BCAT1-KO were stained with 5  $\mu$ L DiD (1mg/mL in DMSO, Biotium, 60,014) for 30 min at 37°C and 500 cells/well were seeded on 80–100 $\mu$ L low-melting agarose in 96-well plates. To promote spheroid formation, cells were maintained for 48 h in Neurobasal medium (Life Technologies, 10888022) supplemented with B27 (Gibco, 12587010), EGF (Gibco, PHG0311) and FGFb (Biomol, 5036150). Brains were obtained from 8–12 weeks old male C57BL6 mice. Immediately after extraction, the brains were placed in PBS and cut into 350  $\mu$ m thick slices (speed = 0.22 mm/s, amplitude = 1) using a vibratome (Leica VT1200S). The slices were placed on 6-well membrane inserts and cultured in brain-slice medium MEM (ThermoFisher Scientific, 31,095-029) with 25% horse serum, 1mM L-glutamine, 100U/mL penicillin/streptomycin, 25mM HEPES (Sigma Aldrich, H0887-20ML), 5mg/mL D-glucose (Sigma Aldrich, G8644-100ML) at 37°C, 5%  $\text{CO}_2$ . To prevent brains from drying, a drop of medium was added to each brain slice and the medium under the insert was refreshed daily. Spheroids of similar size were collected and implanted into the brain slices using a blunt Hamilton syringe (Merck, 701N) under a binocular microscope. Approximately 8–10 spheroids were injected along the cortex of each brain slice. After implantation, the brain slices were cultured for additional 48h after and fixed in 4% PFA (ThermoFisher Scientific, 28,908). The tissue was optically cleared using serial dilution of D-fructose (115%–20% w/v) in water with 0.5%  $\alpha$ -Thioglycerol (Sigma Aldrich, M1753). The slices were incubated in each solution 4–24h at RT with gentle shaking and imaged using a fluorescence microscope with the Cy5 channel. z stack series of each spheroid was obtained with 10  $\mu$ m stacks and processed using the Extended Depth of Focus (EDF) module included in the Nikon's NIS software. The images were analyzed using ImageJ software by quantifying the total area of the invading cells, excluding the area of the spheroid.

### QUANTIFICATION AND STATISTICAL ANALYSIS

Statistical significance was calculated for experiments for which at least 3 biological replicates were performed. Data are presented as mean  $\pm$  SEM. p-values were determined using unpaired, two-tailed Student's *t* test (except specified in the text). For the *in vivo* experiments, the significance of the survival difference between the groups (N = 8 mice) was calculated using the Log Rank test with no censored events.